CHAPTER 4

Terahertz Semiconductor Quantum Well Photodetectors

J. C. Cao* and **H. C. Liu†**

Contents

1. INTRODUCTION

THz detectors are one of the key devices in various THz applications, such as THz science research, bio and chemical material identification, medical imaging, security screening, and communication (Ferguson and Zhang, 2002). Early THz detectors are thermal detectors and semiconductor

* Key Laboratory of Terahertz Solid-State Technology, Shanghai Institute of Microsystem and Information Technology, Chinese Academy of Sciences, 865 Changning Road, Shanghai 200050, China

† Key Laboratory of Artificial Structures and Quantum Control, Department of Physics, Shanghai Jiao Tong University, 800 Dongchuan Road, Shanghai 200240, China

Semiconductors and Semimetals, Volume 84
ISSN 0080-8784, DOI: 10.1016/B978-0-12-381337-4.00004-8

Semiconductors and Semimetals, Vol 84, 2011, pp. 195–242.

photoconductive detectors (Haller, 1994). Thermal detectors include Lithium tantalate ($LiTaO_3$) pyroelectric detector (Byer *et al.*, 1975; Fukada and Furukawa, 1981), deuterated triglycine sulfate (DTGS) pyroelectric detector (Goss *et al.*, 1984; Lal and Batra, 1993), and Si bolometer (Downey *et al.*, 1984; Richards, 1994). Doped Ge photoconductive detector (Haller, 1994; Haller *et al.*, 1979), n type bulk GaAs detector (Gornik, 1984), and homojunction and heterojunction interfacial workfunction internal photoemission (HIWIP and HEIWIP) far-infrared detectors (Perera, 2006; Perera *et al.*, 2000) are typical semiconductor photoconductive detectors. These devices are used in astronomy and astrophysics (Haller, 1994); besides, DTGS and Si bolometer are used in FTIR to measure the transmission and reflection spectra of materials or the emission spectra of lasers. $LiTaO_3$ detectors are used to calibrate the laser-emission power (Li. *et al.*, 2009a), and the array of which can also be used to characterize and analyze the beam of lasers or image (Yang *et al.*, 2008). Recently, using intersubband transitions in semiconductor quantum structures, THz quantum well photodetectors (THz QWPs) have been demonstrated as fast, compact, and easy integratable THz photon detectors (Cao, 2006; Cao *et al.*, 2006; Chen *et al.*, 2006; Graf *et al.*, 2004; Guo *et al.*, 2009; Lake *et al.*, 1997; Liu *et al.*, 2008, 2004; Luo *et al.*, 2005; Patrashin *et al.*, 2006; Tan and Cao, 2008; Tan *et al.*, 2010, 2009). Compared with THz thermal detectors, THz QWPs are narrowband and fast response, which are suitable for laser-emission characterization and THz communication (Grant *et al.*, 2009).

As the extension of quantum well infrared photodetectors (QWIPs) in THz range, THz QWPs have similar device performance and characteristics with QWIPs. Based on GaAs/AlGaAs material system, there are two types of QWIPs: photoconductive QWIP and photovoltaic QWIP. Reported THz QWPs are mostly photoconductive detectors (Guo *et al.*, 2009; Liu *et al.*, 2004; Luo *et al.*, 2005; Patrashin *et al.*, 2006). Because of good responsivity and high sensitivity, photoconductive QWIPs are widely used in focal plane arrays and multicolor detection (Gunapala *et al.*, 2000), while photovoltaic QWIPs, which are low-dark current (Schönbein *et al.*, 1996), working at zero or near-zero bias and only existing in midinfrared range (Schneider *et al.*, 1996, 1997) so far, can be used to construct high thermal resolution focal plane array (Schneider *et al.*, 2003).

In this chapter, the working mechanism, simulation, design, and characterization of THz QWPs are discussed systematically. Then, we introduce some recent applications based on THz QWPs.

2. PRINCIPLE OF THz QWP

In 1985, infrared absorption by intersubband transition in GaAs/AlGaAs multiple quantum well was first observed by West and Eglash (1985). After

that, a new photon-detection technology based on intersubband transition in quantum well was realized and studied by many researchers (Levine, 1993; Levine *et al.*, 1990, 1987; Schneider *et al.*, 2003). THz QWPs are the extension of QWIP to THz range. In 2004, Liu *et al.* (2004) realize the first THz QWP. Since then, significant improvements in simulation and design of active region (Guo *et al.*, 2009; Liu *et al.*, 2007a; Xiong *et al.*, 2008), device performance (Hewageegana and Apalkov, 2008; Luo *et al.*, 2005; Patrashin and Hosako, 2008; Schneider *et al.*, 2009), and applications (Fathololoumi *et al.*, 2010; Graf *et al.*, 2009; Luo *et al.*, 2006) have been achieved.

According to different active region structures, electron distributions, and transport mechanisms, there are two types of quantum well photodetectors: photoconductive and photovoltaic. The active region consists of periodic multiple quantum wells and barriers. Each period include a doped GaAs layer (well) and a AlGaAs layer (barrier). The operation mechanism of THz QWPs is as follows: when THz waves are incident on the active part of the detectors, the electrons on the bond state in the quantum well absorb the THz photons and then get excited to the quasicontinuum state, which is very close to the top of the barrier. With external bias, these excited carriers (electrons) result in a photocurrent. The response peak is determined by the energy-level spacing between the bond state and quasicontinuum state, which can be tailored by barrier height, well width, and doping density in the well. Usually, many wells (10–100) are required for sufficient absorption. Conductive THz QWPs are promising detectors in future high-speed THz wireless communication because of their simple structure and high respond speed.

Because of different doping types, conductive THz QWPs can either be n-type or p-type. In quantum wells, electrons are bound to the well only in the growth direction of quantum wells; while in the direction normal to the growth direction, the dispersion relation of electron is parabolic under effective mass approximation for n-type, which is similar to free electrons. Hence, n-type quantum wells can not absorb photons of normal incident light, while p-type quantum wells can as a result of intervalence transitions of holes. So, 45° incident, light-coupling geometry or grating coupler is often used in n-type devices, and normal incident can be directly used in p-type ones. However, because of other limitations such as low mobility, the performances of p-type devices are far inferior to n-type ones. Recently, many advances of n-type THz QWPs have been obtained (Guo *et al.*, 2009; Liu *et al.*, 2007a; Luo *et al.*, 2005; Patrashin *et al.*, 2006; Schneider *et al.*, 2009).

Detector responsivity is an important performance characteristic, usually written as (Beck, 1993; Liu, 1992)

$$\mathcal{R}_{\mathrm{i}} = \frac{I_{\mathrm{photo}}}{\hbar\omega\Phi} = \frac{e}{\hbar\omega}\eta g_{\mathrm{photo}}, \tag{4.1}$$

where ω and Φ are the frequency and the number of the incident photon per unit time, respectively, $\eta = N\eta^{(1)}$ is the total absorption quantum efficiency, in which $\eta^{(1)}$ is the absorption quantum efficiency of single quantum well, and N is the number of quantum wells in active region. g_{photo} is the photoconductive gain, which is

$$g_{\text{photo}} = \frac{\tau_{\text{relax}}}{\tau_{\text{esc}} + \tau_{\text{relax}}} \frac{\tau_{\text{trans}} + \tau_{\text{c}}}{\tau_{\text{trans}}} \frac{1}{N} = \frac{p_{\text{e}}}{p_c} \frac{1}{N}, \tag{4.2}$$

where τ_{relax} and τ_{esc} are the intersubband relaxation time and the escape time from the quantum well, respectively. p_{c} and p_{e} are trapping or capture probability when electrons with higher energy than barrier pass through the quantum wells and the escape probability when excited electrons escape the quantum wells, respectively.

Detectivity $D^{\star}$ and blip (background limited infrared performance) temperature are the two most important THz QWP characteristics. $D^{\star}$ is the signal (per unit incident power) to noise ratio normalized by the detector area and the measurement electrical bandwidth. The relevant noise contributions are from (1) the detector itself (i.e., dark current) and (2) the fluctuation of the photocurrent induced by background photons incident on the detector.

When the noise is only because of dark current, using three-dimensional (3D) carrier drift model and two-dimensional (2D) emission-capture model (Schneider and Liu, 2006), we get the detector noise limited $D^{\star}$

$$D^{\star}_{\text{det}} = \frac{\lambda}{2\pi\hbar c} \frac{\eta}{\sqrt{N}} \sqrt{\frac{\tau_{\text{c}}}{N_{\text{3D}} L_{\text{p}}}}, \tag{4.3}$$

and

$$D^{\star}_{\text{det}} = \frac{\lambda}{2\pi\hbar c} \frac{\eta}{\sqrt{N}} \sqrt{\frac{\tau_{\text{scatt}}}{N_{\text{2D}}}}, \tag{4.4}$$

where λ is the wavelength, N_{3D} and N_{2D} can be approximated by

$$N_{\text{3D}} = 2\left(\frac{m_{\text{b}} k_{\text{B}} T}{2\pi\hbar}\right)^{3/2} \exp\left(-\frac{2\pi\hbar c}{\lambda_{\text{c}} k_{\text{B}} T} + \frac{E_{\text{f}}}{k_{\text{B}} T}\right), \tag{4.5}$$

and

$$N_{\text{2D}} = \frac{m k_{\text{B}} T}{\pi\hbar^2} \exp\left(-\frac{2\pi\hbar c}{\lambda_{\text{c}} k_{\text{B}} T} + \frac{E_{\text{f}}}{k_{\text{B}} T}\right), \tag{4.6}$$

where m (m_b) is the effective mass in the well (barrier), and λ_c is the cutoff wavelength. Fermi energy and the electron density in quantum well satisfy

$$N_D = (m/\pi\hbar^2)E_f. \tag{4.7}$$

In view of the balance between scattering escape and capture, Eq. (4.3) and (4.4) are actually equivalent. However, they do show the physical process from different perspectives. While Eq. (4.3) relates the detectivity to the 3D effective carrier concentration and the capture process, Eq. (4.4) addresses a 2D effective carrier concentration and a scattering (or emission) process. From Eqs. (4.3)–(4.6), the expected general behavior for a photoconductor is seen, such as (1) a higher η or lower T lead to a higher $D^\star$, and (2) λ_c and T are the most sensitive parameters, being on the exponent. Noting that η is proportional to the doping density and hence the Fermi energy, there is an optimum value for E_f. The optimum value is found by

$$\frac{d}{dE_f}\left[E_f \exp(-\frac{E_f}{2k_BT})\right] = 0, \tag{4.8}$$

which gives the maximum $D^\star$ when $E_f = 2k_BT$ (Kane *et al.*, 1992). This condition dictates an optimum value for N_D for maximizing $D^\star$.

The blip condition is defined when the photocurrent caused by the background equals the dark current, and the temperature is called blip temperature (T_{blip}). For operations at and lower than T_{blip}, the detector is said to be under blip condition, and then the maximum detectivity is limited by the background.

In the blip regime, the background limited $D^\star_{det}$ is given by

$$D^\star_{blip} = \frac{\lambda_p}{4\pi\hbar c}\sqrt{\frac{\eta_p}{\phi_{B,\,ph}}}, \tag{4.9}$$

where λ_p is the peak detection wavelength, η_p is the peak absorption, and $\phi_{B,ph}$ is the integrated background photon number flux (per unit area) incident on the detector. For a given wavelength and if a detector is blip, $D^\star_{det}$ only depends on the absorption quantum efficiency and the background photon flux. The electron lifetime becomes irrelevant in this regime. Using three-dimensional (3D) carrier drift model and two-dimensional (2D) emission-capture model, the blip temperature is found to be determined by the following equations:

$$\eta^{(1)}\tau_{scatt}\phi_{B,\,ph} = \left(\frac{mk_BT}{\pi\hbar^2}\right)\exp\left(-\frac{2\pi\hbar c}{\lambda_c k_BT} + \frac{E_f}{k_BT}\right), \tag{4.10}$$

and

$$\eta^{(1)}\tau_c\phi_{B,\,ph} = 2\left(\frac{m_b k_B T}{2\pi\hbar^2}\right)^{3/2} L_p \exp\left(-\frac{2\pi\hbar c}{\lambda_c k_B T} + \frac{E_f}{k_B T}\right), \tag{4.11}$$

where $\eta^{(1)}$ is the peak absorption efficiency for one quantum well.

From Eqs. (4.10) and (4.11), the most sensitive parameter is λ_c, being in the exponent. A high capture velocity (short scattering time), although giving rise to a fast intrinsic response speed, leads to a low T_{blip}. It is interesting to note that T_{blip} depends on the one well absorption, not the total absorption, and that improving $\eta^{(1)}$ has the same effect as improving τ_c/L_p and τ_{scatt}. The practical values of τ_c for QWIPs fall in the range of 1–10 ps. Given λ_c, τ_c, T, and $\phi_{B,\,ph}$, Eq. (4.10) can be rewritten as

$$\frac{E_f}{k_B T}\exp\left(-\frac{E_f}{k_B T}\right) = (\text{Constant}) \times \exp\left(-\frac{2\pi\hbar c}{\lambda_c k_B T}\right). \tag{4.12}$$

Noting $\eta^{(1)} \propto N_D \propto E_f$, one can adjust E_f to maximize the left-hand-side of the equation, which maximizes T_{blip}. The optimum condition is $E_f = k_B T$, which is different from the optimum condition for maximizing the detector limited detectivity by a factor of two (i.e., $E_f = 2k_B T$). These predictions have been verified experimentally for QWIPs in the 8–10 μm region (Yang *et al.*, 2009).

For completeness, the ideal (blackbody) background photon flux is given by

$$\phi_{B,\,ph} = \int d\lambda \left[\pi \sin^2(\theta/2)\right] \eta(\lambda) L_B(\lambda), \tag{4.13}$$

where θ is the field of view (FOV) full-cone angle, the photon irradiance is given by

$$L_B(\lambda) = \frac{2c}{\lambda^4}\left[\exp\left(\frac{2\pi\hbar c}{\lambda k_B T_B}\right) - 1\right]^{-1}, \tag{4.14}$$

where T_B is the background temperature, and the device spectral lineshape is modeled by

$$\eta(\lambda) = \frac{1}{1 + \left(\frac{\Delta\lambda}{2\lambda} - \frac{\Delta\lambda}{2\lambda_p}\right)^2}. \tag{4.15}$$

Presently, most THz QWPs are photoconductive detectors, covering peak response frequency from 2 to 7 THz. The operation temperature is still not very high, about 30 K or lower (Liu *et al.*, 2007a).

3. THEORY AND SIMULATION OF THz QWP

3.1. Basics of simulation models

THz QWPs are designed with the same principle used in midinfrared quantum well photodetectors. Quantum well photodetector is a unipole device, which replies on intersubband transitions of electrons (holes). Understanding the transport is important to predict the detector performance. Several models have been proposed: (1) nonequilibrium Green function based on quantum transport theory (Lake *et al.*, 1997) and (2) Monte Carlo method based on Boltzmann equation. Ryzhii *et al.* (1998) used this method to study the dark current, I–V characteristic and the nonlinear dynamics of carrier transport; Cellek *et al.* (2004) applied a microscopic scattering model in the Monte Carlo simulation to solve the problem of transition between local state and extented state; (3) rate equation method based on quasimicroscopic scattering model. Jovanović *et al.* (2004) used this method to analyze the gain, photocurrent response, and I–V characteristic of quantum well photodetectors.

Various scattering mechanisms and physics effects can be easily included in the nonequilibrium Green function method, such as correlation, depolarization and memory effect, and so on. But this method is difficult to solve for complex structures because of its heavy computational demand. Rate equations take into account microscopic scattering mechanisms, but the quantitative results are still difficult to obtain because of phenomenological parameters. Different scattering processes can be conveniently considered with Monte Carlo method. Considering all these factors, Monte Carlo method is an effective method to design quantum well photodetectors.

The numerical models for dark current include self-consistent drift-diffusion model, self-consistent emission-capture model, and numerical Monte Carlo model. The self-consistent drift-diffusion model developed by Ershov *et al.* (1996, 1995) calculates the QWIP characteristics by self-consistently solving three equations: (1) Poisson equation, (2) continuity equation for electrons in the barriers, and (3) rate equation for electrons in the quantum wells. The inclusion of the Poisson equation is especially important for QWIPs with a small number of wells (<10) because the field can be substantially different (often higher) for the first few periods starting from the emitter in comparison with the rest of the wells. The continuity equation involves the current (expressed in the standard

drift-diffusion form) and rates of thermal and optical generation and of recombination. Using this numerical model, we were able to account for the observed unusual capacitance behavior (Ershov *et al.*, 1997b) and explain the nonlinear photoconductivity at high excitation power using a CO_2 laser (Ershov *et al.*, 1997a). In addition, the model has the capability to predict transient and hence frequency characteristics (Ershov, 1996), as well as photoresponse under localized IR excitation (Ershov, 1998).

Thibaudeau *et al.* (1996) presented a numerical model that extends the simple emission-capture model presented before. The model allows the electric field to be nonuniform, self-consistently determined by Gauss' law. The authors obtained better agreement with experiments than the simple model. Ryzhii (1997) constructed an analytical model by solving Poisson's equation and an equation governing the electron balance in the quantum well. Interesting functional dependencies of the responsivity on the number of wells and the photon excitation power were found. Jovanović *et al.* (2004) constructed a quantum mechanical model considering all scattering processes, including emission and capture. The model results were compared with experimental data on a GaAs/AlGaAs device and good agreement was found.

Ryzhii and Ryzhii (1998) and Ryzhii *et al.* (1998) carried out Monte Carlo simulations on QWIPs, in particular their ultrafast electron-transport properties. Cellek and Besikci (2004) and Cellek *et al.* (2004) also performed such simulations, analyzing the effects of material properties on the device characteristics. They found the evidence that the L-valley in GaAs/AlGaAs QWIPs plays an important role in determining the responsivity versus voltage behavior. Monte Carlo simulations shed light on the hot electron distribution on top of the barriers, and they should provide guidance to the optimization of QWIPs.

To end this section, although several models have been established, with varying degree of complexity, and good agreement between models and experiments has been obtained, to formulate a true first-principle QWIP model is a highly nontrivial task. This is because the QWIP is rather complicated. Given the wide barriers and narrow wells, the transport mechanism falls between ballistic and drift-diffusion; and because of the high doping and high field, realistic calculations of scattering or trapping rates are extremely complicated and have not been performed so far. The situation becomes even more complicated to model for p-type structures (Petrov and Shik, 1998).

3.2. Dark current

Photoconductive THz QWPs have features of simple structure, high-speed response, and high sensitivity, which are suitable for high-speed detection

applications (Cao, 2006). In this section, we will introduce two simple models for the simulation of dark current in photoconductive devices: 3D carrier drift model and 2D emission-capture model; then the dark current curve of a THz QWP is simulated by an improved emission-capture model.

A good understanding of the dark current is crucial for design and optimization of QWIPs because dark current contributes to the detector noise and dictates the operating temperature. There are several common assumptions or approximations made to define the physical regime for all the discussions in this subsection. These are as follows: (1) the interwell tunneling contributes negligibly to the dark current, (2) the electron density in each well remains constant (Liu *et al.*, 1991), (3) the heavily doped emitter serves as a perfectly injecting contact (Liu *et al.*, 1997), and (4) mainly one bound state is confined in the quantum well, including the case where the upper state (final state of the ISBT) is in resonance or very close to the top of the barrier. Assumption (1) is satisfied by requiring the barriers to be sufficiently thick. Assumption (2) is a good approximation but is not strictly valid especially at large bias voltages as shown experimentally (Liu *et al.*, 1991). Assumption (3) is expected to be valid for QWIPs with a large number of quantum wells, consistent with experimental results. The effect of contacts becomes important for QWIPs with a small number of quantum wells as shown in simulations (Ershov *et al.*, 1995). To produce good detectors, condition (4) is required (Liu, 1993).

Here we first present two simple physical models, and then the simulation results are compared with experimental data.

1. 3D carrier drift model: The first physical model calculates J_{dark} by directly estimating j_{3D}. A 3D electron density on top of the barriers N_{3D} is estimated with only the drift contribution taken into account (diffusion is neglected). The model was first presented in a very clear and concise article by Kane *et al.* (1992). The dark current density is given by

$$J_{\text{dark}} = eN_{3D}\upsilon(F), \tag{4.16}$$

where $\upsilon(F)$ is the drift velocity as a function of electric field F. The drift velocity takes the usual form

$$\upsilon(F) = \frac{\mu F}{\left[1 + (\mu F/\upsilon_{\text{sat}})^2\right]^{1/2}}, \tag{4.17}$$

where μ is the low field mobility and υ_{sat} is the saturated drift velocity. Usually THz QWPs are degenerately doped in the wells, i.e., the top of the Fermi sea is higher than the energy of the lowest subband, so the only 2D quantum well effect comes into the picture for the evaluation of the Fermi

energy E_f. Assuming a complete ionization, the 2D doping density N_D equals the electron density within a given well, as a good approximation.

2. Emission-capture model: Scattering-assisted escape is the dominant process for a typical QWIP, especially at low fields (Schneider and Liu, 2006). Electrons associated with the confined ground state in the well and distributed on the 2D in-plane dispersion curve undergo a scattering event to get out of the well and then become a 3D mobile carrier in the barrier.

The escape current density can be written as

$$j_e = \frac{eN_{2D}}{\tau_{scatt}}, \tag{4.18}$$

where N_{2D} is a 2D electron density which only includes electrons on the upper part (with energy greater than the barrier height) of the ground state subband and τ_{scatt} is the scattering time to transfer these electrons from the 2D subband to the nonconfined continuum on top of the barrier. The standard THz QWPs having their barriers much wider than wells, we neglect any superlattice miniband effects. The capture probability is related to the relevant time constants by

$$p_c = \frac{\tau_{trans}}{\tau_{trans} + \tau_c}, \tag{4.19}$$

where τ_c is the capture time for an excited electron back into the well, and τ_{trans} is the transit time for an electron across *one* quantum well region including the surrounding barriers. In the limit of $p_c \ll 1$, i.e., $\tau_c \gg \tau_{trans}$, as is true for actual devices at operating electric fields, the dark current becomes

$$J_{dark} = e\frac{N_{2D}}{L_p}\frac{\tau_c}{\tau_{scatt}}\upsilon(F), \tag{4.20}$$

where L_p is the period length of the multiple quantum well structure, which is the sum of the well and barrier widths $L_p = L_w + L_b$. The quantity N_{2D}/τ_{scatt} represents the thermal escape or generation of electrons from the quantum well, and $1/p_c$ is directly proportional to the photoconductive gain.

We theorectically simulated the dark current curves of THz QWP (ID: V267) (Tan *et al.*, 2009). The bias range is from 0.1 to 30 mV, and the temperatures are from 7 to 20 K. In the simulation, the saturated mobility is taken as $\upsilon_{sat} = 1 \times 10^7$ cm/s; the energy of the ground state is $E_1 = 4.25$ meV; the barrier height is $E_b = 0.87x$ eV; and the effective mass of electron is

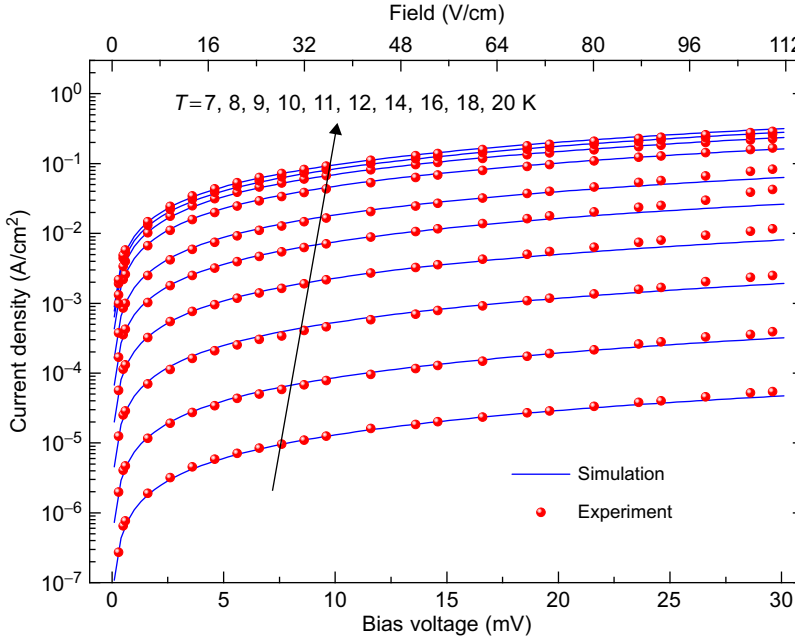

FIGURE 4.1 The I–V curves. Solid lines: mumerical results; dots: experimetal data.

$m^* = 0.067m_e$ and $m_b = (0.067 + 0.083x)m_e$, where x is the Al fraction of the barrier. The dark current curves are shown in Fig. 4.1, where the theoretical results (solid lines) agree well with the experimental measurements (dots) (Tan *et al.*, 2009). In the temperature range of 7 to 20 K, the dark current of V267 increases quickly with increasing temperatures. The range of the current density is from 10^{-5} to 10^{-1} A/cm^2 within the bias range. The relation between dark current and temperature indicates that the thermionic emission is the mainly dark current mechanism in THz QWP (Çelik *et al.*, 2008; Tan *et al.*, 2009).

In the simulating process for the dark currents, it is important to note that a temperature-dependent mobility parameter was used to fit the I–V curves. The fitted mobility versus temperature relation is shown in Fig. 4.2, having a decreasing trend with temperature. This is opposite to the Hall mobility (Stillman *et al.*, 1970), which is of an ionized impurity scattering origin in the relatively pure GaAs materials at the temperature less than 20 K. The reason for the discrepancy is surely related to the simplicity of the model, neglecting processes such as field nonuniformity and self-consistency.

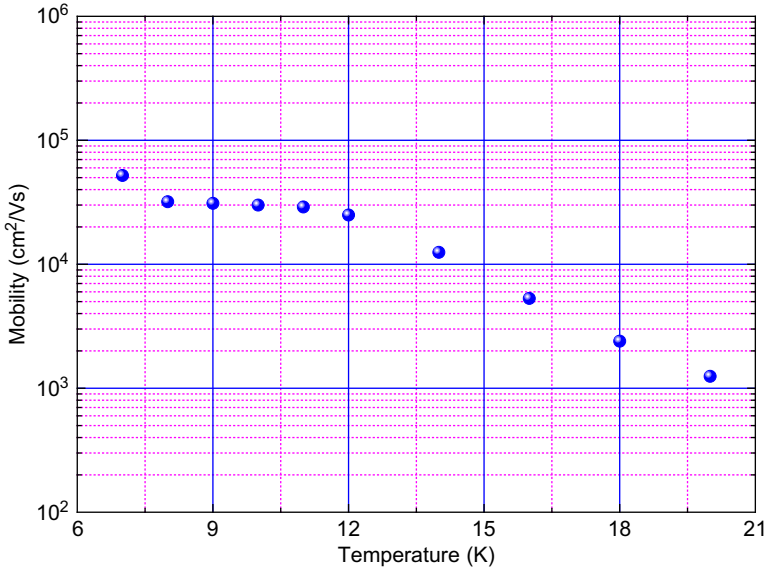

FIGURE 4.2 Vertical electron drift mobilities in the device structure versus device temperatures (Tan *et al.*, 2009).

3.3. Photocurrent

The distinct feature of photoconductive QWPs in contrast with the conventional intrinsic and extrinsic photoconductors is the discreteness, i.e., incident photons are only absorbed in discrete quantum wells that are normally much narrower than the inactive barrier regions. In this section, we discuss the photocurrent caused by intersubband excitations in a QWP.

The photocurrent spectrum is an important characteristic of the device performance, which gives the peak response frequency and the sensitivity to the radiation. Compared with the wideband IR sources (such as Globar, Hg lamp, and so on), THz QWPs are narrowband detectors.

We calculated the spectral response of a THz QWP designed for 7 THz detection peak frequency (Cao *et al.*, 2006). We incorporate the effect of GaAs optical phonons which give rise to a strong absorption in the region of 34–36 meV and result in an increase in reflection because of the large refractive change around this region. Comparing the calculated spectral shape with experiments, we show the improvement over the standard expressions.

For QWPs, the total absorption coefficient η is usually defined as the ratio of the absorbed electromagnetic energy per unit time, volume, and the intensity of the incident radiation. For simplicity, we define a dimensionless absorption coefficient normalized by the area A instead of

the volume. The expression for η is given by

$$\eta = \frac{\hbar\omega}{IA}\sum_{n,n'}\sum_{k\perp}| < n|(e/m^*)\mathbf{A}\cdot\mathbf{P}|n' > |^2 \times [f(E_n(\mathbf{k}_\perp)) - f(E_{n'}(\mathbf{k}_\perp))] \times \delta(E_{n'}(\mathbf{k}_\perp) - E_n(\mathbf{k}_\perp) - \hbar\omega), \tag{4.21}$$

where I is the intensity of the incident radiation and is given by

$$I = (1/2)\varepsilon_0 c n_0 E_0^2. \tag{4.22}$$

Here n_0 is the refractive index of the material, taken to be real and constant, and E_0 is the electric field amplitude (Liu and Capasso, 2000). Expressing $\mathbf{A}$ by E_0 and changing the summation into a two-dimensional integration (Liu and Capasso, 2000), we get

$$\eta = \frac{\pi e^2}{\varepsilon_0 c n_0 \omega m^{*2}}\sum_{n,n'}\frac{2}{(2\pi)^2}\int d^2k_\perp| < n|p_z|n' > |^2 \cdot [f(E_n) - f(E_{n'})]\delta(E_n - E_{n'} - \hbar\omega). \tag{4.23}$$

The spectral current responsivity $\Re_i$ is given by

$$\Re_i = I_{photo}/(\hbar\omega\Phi_i), \tag{4.24}$$

where Φ_i is the incident photon number per unit time. The photocurrent I_{photo} is given by

$$I_{photo} = i^{(1)}_{photo}/p_c, \tag{4.25}$$

where

$$i^{(1)}_{photo} = e\Phi_i\eta p_e/N \tag{4.26}$$

is the photoemission current directly ejected from one well, N is the number of quantum wells, p_c is the capture probability, and p_e is the escape probability for an excited electron from the well (Liu and Capasso, 2000). Using Eqs. (4.25) and (4.26), we get

$$\Re_i = \frac{e}{\hbar\omega}\eta g_{photo}, \tag{4.27}$$

where photoconductive gain is $g_{photo} = p_e/p_c N$.

Until now, we have assumed that the amount of absorption is the same for all the wells and the absorption by the lattice is negligible (Ershov *et al.*, 1999; Jovanović *et al.*, 2004). However, this assumption does not hold for the present case. In the reststrahlen region (34–36 meV), the absorption by the optical phonons of GaAs is very strong, and the amount of absorption for each well is not the same either. Therefore, Φ_i in Eq. (4.26) should be replaced by $\Phi(z)$, to take into account the difference between the incident light and the light propagating in the QWIP. For simplicity, we take the absorption of the middle well as the average absorption, and use the light intensity I instead of the photon number Φ, $I = \hbar\omega\Phi$, then we have

$$\Re_i = \frac{e\eta I(z)}{\hbar\omega I_i} g_{\text{photo}}. \tag{4.28}$$

Using the following standard expressions (Klingshirm, 1997), $I(z) = I(z = 0)e^{-2\omega k(\omega)z/c}$, $I(z = 0) = (1/2)\varepsilon_0 cn(\omega)E_0^2$ and $I_i = (1/2)\varepsilon_0 cn_i E_0^2$, and $I_i = (1/2)\varepsilon_0 cn_i E_0^2$, where z is the distance from the middle well to the first well, n_i is the refractive index of air, and $n(\omega)$ is the refractive index of the matter in connection with Snells, law of refraction.

If we use a "single oscillator" model to simulate such absorption behavior in the reststrahlen region (Blakemore, 1982), we can easily get the complex refractive index

$$\kappa^*(\omega) \equiv (\kappa_1 - i\kappa_2) = \kappa_\infty + \frac{\omega_{\text{TO}}^2(\kappa_0 - \kappa_\infty)}{\omega_{\text{TO}}^2 - \omega^2 + i2\pi\gamma_p\omega}, \tag{4.29}$$

where κ_0 is the low–frequency dielectric constant, κ_∞ is the high–frequency (optical) dielectric constant, ω_{TO} is the resonant frequency, and γ_p is the damping coefficient. In addition, we have

$$n(\omega) = (1/\sqrt{2})[(\kappa_1^2 + \kappa_2^2)^{1/2} + \kappa_1]^{1/2}, \tag{4.30}$$

$$k(\omega) = (1/\sqrt{2})[(\kappa_1^2 + \kappa_2^2)^{1/2} - \kappa_1]^{1/2}. \tag{4.31}$$

Figure 4.3 shows the spectral variation of the real refractive index $n(\omega)$ and the extinction coefficient $k(\omega)$ for GaAs at $T = 8$ K, yielded from Eqs. (4.30) and (4.31) with $\hbar\omega_{\text{TO}} = 33.81 \times (1 - 5.5 \times 10^{-5}T)$ meV, $\kappa_\infty = 10.88$, $\kappa_0 = \kappa_\infty \times 1.170 \times (1 + 3.0 \times 10^{-5}T)$ (Blakemore, 1982), and $2\pi\hbar\gamma_p = 0.25$ meV. The curves of $n(\omega)$ and $k(\omega)$ cross at the energy $\hbar\omega_{\text{TO}}$ (33.3 meV), and again at the energy $\hbar\omega_{\text{LO}}$ (36.2 meV).

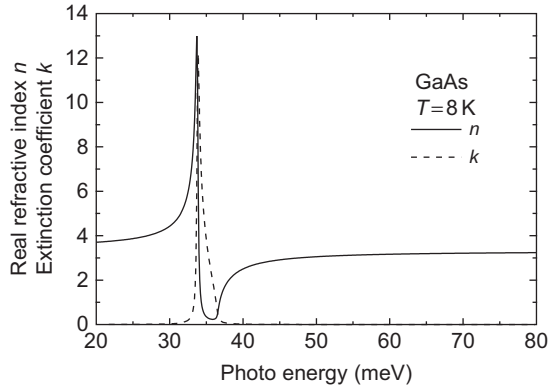

FIGURE 4.3 Spectral variation of the real refractive index and the extinction coefficient for GaAs at 8 K (Cao *et al.*, 2006), modeled by Eqs. (4.30) and (4.31).

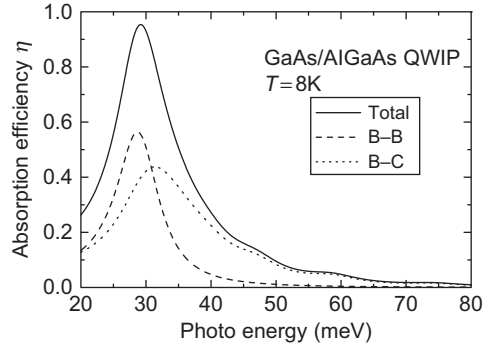

FIGURE 4.4 Calculated absorption quantum efficiency versus photon energy for one well with well width $d = 12$ nm and electron density 10^{17} cm^{-3} (Cao *et al.*, 2006).

In the experiment of THz QWIP (Liu *et al.*, 2004) discussing the reststrahlen region, the device consists of 50 quantum wells made of 12-nm GaAs wells and 40-nm $Al_{0.05}Ga_{0.95}As$ barriers. The center 10-nm region of the wells was doped with Si to 10^{17} cm^{-3}. The 45° edge facet geometry was used for photoresponse measurement and the polarization is p. The applied voltage is only ±0.4 V and the voltage drop across a given well is less than 2 meV, which is negligible compared with the ground-state energy. The absorption spectrum is calculated at zero bias as an approximation (Liu *et al.*, 2004). First, the absorption coefficient is calculated using Eq. (4.23) (Ikonic *et al.*, 1989; Liu, 1993), as shown in Fig. 4.4. Here the ground state energy $E_0 = 14.2$ meV, and the first excited state energy $E_1 = 43.1$ meV is very close to the barrier height V_b. This optimum

design (Liu and Capasso, 2000) will bring both a large absorption and a rapid escape for the excited electrons. From the results of the calculation, we can see that the peak detection wavelength (42.5 μm) is in good agreement with the design, and both bound-to-bound and bound-to-continuum intersubband transitions contribute to the absorption.

Using Eq. (4.28), we get the calculated detector response shown in Fig. 4.5, where the reststrahlen region (34–36 meV) is clearly seen. Comparing with experiments, the general shapes are similar and our model, therefore, indeed represents an improvement over the standard expressions. As an approximation, the calculated absorption spectrum at zero bias is used. For the experiment, the bias voltage is low (given in Liu *et al.* (2004). The polarization is p and the angle is 45°. Comparing experimental and theoretical results in Fig. 4.5, quantitatively there is still a significant difference in the relative response magnitudes above and below the reststrahlen region. We point out that there are uncertainties in both experiment and calculation. In the experiment, the overall shape and the relative strength depend on how well the spectrometer system response is corrected. This is done by using a reference detector assumed to have a flat response, which is not very accurate over a wide spectral range. For the calculation, the barrier height (band offset) has not been tested in this very-low aluminum fraction regime. The barrier height value will

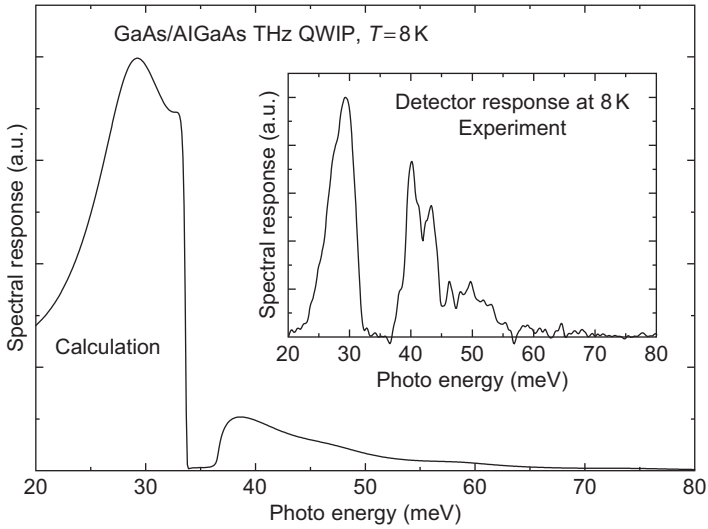

FIGURE 4.5 Calculated and experimental photoresponse spectrum versus photon energy (Cao *et al.*, 2006). The THz QWIP consists of 50 quantum wells made of 12-nm GaAs wells and 40-nm $Al_{0.05}Ga_{0.95}As$ barriers.

change the relative strength of contributions from bound-to-bound and bound-to-continuum transitions, and therefore change the overall shape. Moreover, many-body effects have not been included, which would have moved the overall response to a higher energy and made a better fit in the low-energy region (20–25 meV). In the experimental curve, there are some smaller features, for example, dips at 42 and 45 meV. These may be caused by the weaker absorption of two-zone edge and AlAs-like phonons, and they may also be caused because of the absorption associated with the localized vibrational modes of Si-doped GaAs. A lot of investigations have been done on the absorption induced by Si-related defects in doped GaAs (Chen *et al.*, 1980; Spitzer and Panish, 1969), and the frequencies of all the absorption bands of interest in their study is from 350 to 480 cm^{-1} (43.4–59.6 meV). In addition, there may be absorption resulting from other localized phonon modes (Shen, 1984). We note that having an intersubband transition in resonance with optical photons may lead to a strong coupling and the formation of intersubband polarons. However, because the doping density in the device analyzed here is not high and the intersubband oscillator strength is not large because of the bound-to-quasibound nature, the polaron splitting is expected to be about 1 meV or less (Liu *et al.*, 2003). We, therefore, neglect the effect of strong coupling.

A more detailed comment is in order regarding the AlAs-like phonons. For alloys like AlGaAs, a more complex dielectric function should be used to describe a two-mode oscillator for GaAs-like and AlAs-like optical phonons. However, if we take a simple model of either additive or factorized functions for the entire multiple quantum well stack, a very-strong absorption would also result in the AlAs-like phonon region, which does not agree with experiment. This is an issue to be resolved, i.e., how to include the contribution of the AlAs-like phonon.

In conclusion, we have calculated and discussed the response spectrum of a THz QWP. Because of the optical phonon absorption in the reststrahlen region, the refractive index n and the extinction coefficient k change strongly. Considering all the changes, we have improved the usual expression for $\Re_i$, and obtained better agreement with experiments.

3.4. Many-body effects

Because of the low-doping density, the many-body effects are usually neglected in the design of midinfrared QWPs (Schneider and Liu, 2006). However, for THz QWPs, because the energy difference between the bound subband and the continuum is around 10 meV, notable error of photoresponse peak position will be introduced without considering the many-body effects (Liu *et al.*, 2004; Schneider and Liu, 2006). The many-body effects include the interactions among electrons and between electrons and

other quasiparticles. Earlier investigations have shown that in QWIPs, the electron–electron interactions can affect the optical response peak position (Schneider and Liu, 2006). The other many-body interactions have influence on the linewidth and line shape of photocurrent spectrum (Xiong *et al.*, 2008). We studied the many-body effects on THz QWPs (Guo *et al.*, 2009). It is found that large differences between theory and experiment are introduced without including the above many-body interactions in the theoretical design. Our numerical results show that it is very important to consider the many-body interactions for designing THz QWPs.

In general, because of the large degrees of freedom of a many-particle system, many-body effects can only be treated with various approximation methods. For electron–electron interactions, the static exchange-correlation and the dynamical depolarization (or local field) (Liu, 1994; Załużny, 1993) and exciton-like effects are considered with local density approximation (LDA) within the framework of density functional theory. The depolarization and exciton-like interactions between the ground and excited sublevels are photon-induced many-body contributions (Fung *et al.*, 1999). For the electron–quasiparticle interactions, the electron–phonon and the electron-impurity scatterings are described by using a simple model with two free parameters (Fu *et al.*, 2003; Xiong *et al.*, 2008), the values of which are determined by fitting numerical photocurrent curves to experimental data. Because of the low aluminum concentration in barrier layers, the scattering between electron and interface roughness is not considered.

The photocurrent spectra of two THz QWPs are calculated here; the device parameters are the two devices labeled as V266 and V267 reported in the studies of Liu *et al.* (2004) and Luo *et al.* (2005). Our numerical results show that there is only one bound subband in the quantum well with only the Hartree potential being considered. When the exchange-correlation potential is taken into account, however, two bound subbands exist in the quantum wells for the two THz QWPs, and the second subband is near the top of the barrier. The static exchange-correlation and the dynamical depolarization electron–electron interactions cause blueshifts of the photoresponse peaks, and the calculated photocurrent peak positions agree with the experimental data quantitatively. The shapes of the photocurrent peaks are well described by the energy-dependent Γ model that represents the effects of the electron–phonon and electron-impurity scatterings. The LDA functional for exchange-correlation potential adopted in this chapter cannot properly describe the exciton-like many-body effect in THz QWPs.

The Hamiltonian for an electron in THz QWPs within the effective mass approximation is

$$H = \mathbf{p}\frac{1}{2m^*(z)}\mathbf{p} + V_{\mathrm{QW}}(z) + V_{\mathrm{H}}(z) + V_{\mathrm{xc}}(z), \tag{4.32}$$

where m^* is the electron effective mass, $\mathbf{p}$ is the momentum operator, V_{QW} is the well confinement potential, V_{H} is the Hartree potential, and V_{xc} is the exchange-correlation potential. The wave function of electrons in the THz QWPs is expressed as a two-dimensional plane wave times a one-dimensional envelope function along the growth direction, $\psi_{\mathbf{k},l}\left(\mathbf{r}_{||},z\right) = \exp\left(i\mathbf{r}_{||}\cdot\mathbf{k}_{||}\right)\varphi_{k_z,l}\left(z\right)$, where $\mathbf{r}_{||}$ and $\mathbf{k}_{||}$ are the in-plane coordinate and momentum, k_z is the quasimomentum limited to the first Brillouin zone associated with the quantum well period, and l is the subband index. With the above approximation, the Schrodinger equation reads

$$\left[-\frac{\hbar^2}{2}\frac{\partial}{\partial z}\left(\frac{1}{m^*(z)}\frac{\partial}{\partial z}\right)+V_{\mathrm{QW}}(z)+V_{\mathrm{H}}(z)+V_{\mathrm{xc}}(z)\right]\varphi_{l,k_z}(z)=\varepsilon_{l,k_z}\varphi_{l,k_z}(z). \tag{4.33}$$

The energy of the electron is $E_{k,l}=\hbar^2k_{||}^2/2m^*+\varepsilon_{k_z,l}$. The electron charge density is given by

$$\rho_{\mathrm{e}}\left(z\right)=|e|\sum_{k,l}f\left(E_{k,l},\varepsilon_{\mathrm{F}},T\right)\left|\varphi_{k_z,l}\left(z\right)\right|^2, \tag{4.34}$$

where e is the electron charge, f is Fermi distribution function, ε_{F} is the Fermi energy, and T is temperature. Once the density is known, the Hartree potential V_{H} can be obtained by solving the Poisson equation

$$\frac{\partial^2}{\partial z^2}V_{\mathrm{H}}\left(z\right)=-\frac{\rho_{\mathrm{e}}\left(z\right)-\rho_{\mathrm{d}}\left(z\right)}{\epsilon}, \tag{4.35}$$

where $\rho_{\mathrm{d}}\left(z\right)$ is the fixed ionized dopant density, and ϵ is dielectric constant. In general, it is a difficult task to find the exact exchange-correlation potential V_{xc}. In this chapter, the widely used LDA based on the density functional theory is adopted through the following formula (Gunnarsson and Lundqvist, 1976; Zhang and Potz, 1990):

$$V_{\mathrm{xc}}(z)=\frac{e^2}{4\pi^2\epsilon a_{\mathrm{B}}r_{\mathrm{s}}\left(z\right)}\left(\frac{9}{4}\pi\right)^{1/3}\left[1+0.0545r_{\mathrm{s}}\left(z\right)\ln\left(1+\frac{11.4}{r_{\mathrm{s}}\left(z\right)}\right)\right], \tag{4.36}$$

where $a_{\mathrm{B}}=\epsilon\hbar^2/e^2m^*\left(z\right)$ is the effective Bohr radius and $r_{\mathrm{s}}=\left[\left(3/4\pi\right)\left(a_{\mathrm{B}}^3\rho_{\mathrm{e}}(z)\right)^{-1}\right]^{1/3}$. The band structure of THz QWP is obtained by self-consistently solving the above set of equations with plane-wave expansion method.

The absorption efficiency η can be derived from the Fermi's golden rule

$$\eta(\omega) = \frac{\pi e^2}{\epsilon_0 c n_0 \omega m^{*2}} \sum_j \int \frac{d\mathbf{k}}{(2\pi)^3} \left|\langle j \left| p_z \right| 0 \rangle\right|^2 \times \left[f\left(E_{k,0}, \varepsilon_F, T\right) - f\left(E_{k,j}, \varepsilon_F, T\right)\right] \delta\left(\Delta\widetilde{E}_{k,l,0} - \hbar\omega\right), \tag{4.37}$$

where ϵ_0 is the vacuum permittivity, c is the speed of light, n_0 is the refractive index, and $\Delta\widetilde{E}_{k,l,0}$ is the energy difference between the jth and the ground subbands with depolarization and exciton-like effects included. The expression for $\Delta\widetilde{E}_{k,l,0}$ is (Ando *et al.*, 1982)

$$\begin{aligned}
\Delta\widetilde{E}^2_{k,l,0} &= \Delta E^2_{k,l,0}\left(1 + \alpha_{k,l,0} - \beta_{k,l,0}\right), \\
\alpha_{k,l,0} &= \frac{2e^2\rho_{2D}}{\epsilon \Delta E_{k,l,0}} \int_{-\infty}^{\infty} dz \left[\int_{-\infty}^{z} dz' \varphi_{k_z,l}(z') \varphi_{k_z,0}(z')\right]^2, \\
\beta_{k,l,0} &= -\frac{2\rho_{2D}}{\Delta E_{k,l,0}} \int_{-\infty}^{\infty} dz \varphi_{k_z,l}(z)^2 \varphi_{k_z,0}(z)^2 \frac{\partial V_{xc}[\rho(z)]}{\partial \rho(z)}.
\end{aligned} \tag{4.38}$$

Here $\alpha_{k,l,0}$ and $\beta_{k,l,0}$ describe the depolarization and exciton-like effects, respectively, and $\Delta E_{k,l,0}$ is the energy difference between l and 0 subbands without the two dynamical many-body corrections. The photocurrent is $I_{photo} = e\Phi\eta g_{photo}$, where Φ is the incident photon number per unit time, and g_{photo} is the photoconductive gain. On the assumption of energy-independant Φ and g_{photo}, the photon current I_{photo} is proportional to the absorption efficiency η. For simplicity, the delta function in Eq. (4.37) is replaced by a Lorentzian $\Gamma / \left[\pi\left(E_{k,j} - E_{k,0} - \hbar\omega\right)^2 + \Gamma^2\right]$, where Γ is a small constant. In Fu *et al.* (2003) and Xiong *et al.* (2008), an energy-dependent $\Gamma = a\sqrt{E - \hbar\omega_{TO}} + b$ is used to take into account the effects of electron–phonon and electron-impurity on the shape of photocurrent peak, where a and b are parameters, and E is the electron energy measured from the conduction band edge of (Al,Ga)As barrier. In this chapter, the same expression of Γ is adopted to fit for the experimental results.

The band structures and photocurrents of two THz QWPs are calculated. In order to compare with the experimental results, the parameters of the two THz QWPs, including the barrier and well widths, the barrier height, and the doping concentration and position, are those reported in the studies of Liu *et al.* (2004) and Luo *et al.* (2005). The effective electron mass is $0.067m_0$ with m_0 the electron mass. The temperature is 8.0 K. To expand the envelope wave functions, 99 plane waves are used. The

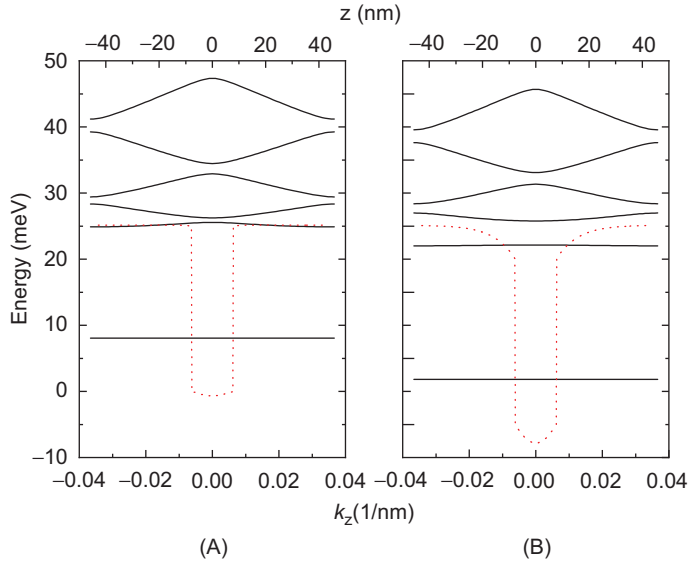

FIGURE 4.6 Band structures of V266 THz QWP (A) without and (B) with exchange-correlations potential (Guo *et al.*, 2009).

convergent criteria is $\left|(\varepsilon_{\mathrm{F}i} - \varepsilon_{\mathrm{F}i-1})/\varepsilon_{\mathrm{F}i}\right| \leqq 0.0005$, with $\varepsilon_{\mathrm{F}i}$ being the Fermi energy at the ith iterative step, and the convergence is reached in the condition of $i \leqq 15$ for all the calculations.

Figure 4.6 shows the band structure of V266 THz QWP with and without the exchange-correlation potential. As shown in Fig. 4.6A, when the Coulomb interaction is taken into account with Hartree approximation, only one localized subband exists in the quantum well. The first excited subband is in resonance with the top of the barrier, which is in accordance with the design rule of bound-to-quasibound QWIPs. However, because the quantum well is very shallow for THz QWPs, the neglect of exchange-correlation potential will introduce large errors in design of THz QWPs. Because the exchange-correlation potential is negative, for V266 THz QWP, the exchange-correlation interaction deepens the quantum well by about 6.3 meV, which makes the first excited subband fall into the quantum well and be off resonance with the top of the barrier. The energy difference between the ground and the first excited subbands increases by about 3.2 meV for V266 THz QWP. Similar effects of exchange-correlation interaction on the band structure of V267 THz QWP (not shown) are found. The effects of Hartree potential on the band structures of V266 and V267 are also explored. Because the Si dopants are doped in well layers, the electrons and ionized dopants are spatially overlapped, which lowers the Hartree contribution. The energy difference between the ground and the

first excited subbands increases by 0.4 meV for V266 and 0.3 meV for V267 with Hartree potential being considered. The calculated results show that the exchange-correlation interaction plays a key role in the design of THz QWPs.

The theoretical and experimental photocurrent spectra for V266 and V267 are shown in Fig. 4.7. In order to obtain some physical insights, different many-body interactions are taken into account step-by-step in our calculations. The energy differences of response peak positions between theory and experiment for V266 and V267 THz QWPs are 5.6meV (24.8%) and 4.8 meV (36.0%) without including any many-body interaction. When the static exchange-correlation potentials are taken into account, the differences decrease to 2.4 meV (10.6%) and 2.6 meV (19.4%), respectively. The further improvements of theoretical response peak positions are achieved by considering the dynamical depolarization effects, and the discrepancies are about 0.2 meV (0.9%) and 1.1 meV (8.2%) for V266 and V267, respectively.

The exciton-like interaction plays a negative role in our calculations. Earlier investigations show that the value of $\beta_{k,l,0}$ is much smaller than that

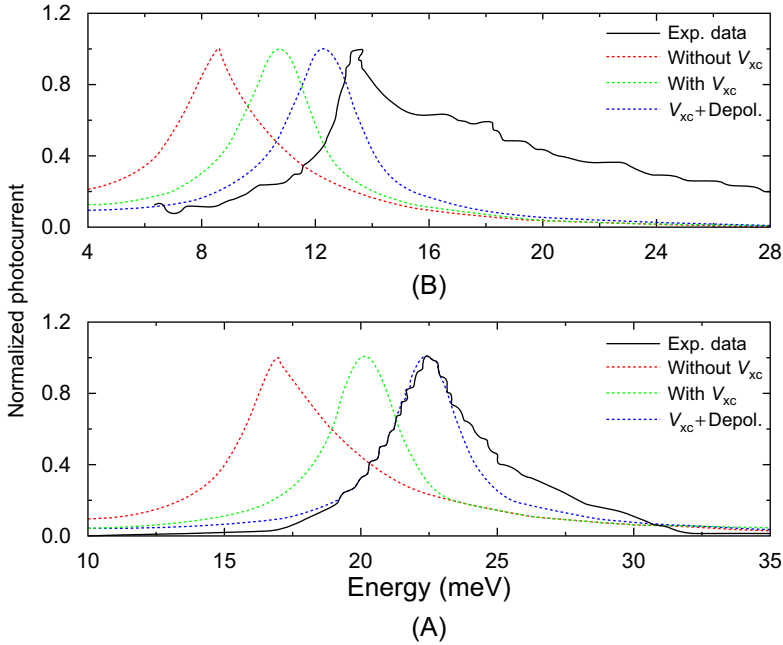

FIGURE 4.7 Calculated and experimental photocurrent spectra of THz QWPs, (A) for V266 THz QWP and (B) for V267 THz QWP (Guo *et al.*, 2009).

of $\alpha_{k,l,0}$ in Eq. (4.38) (Helm, 2000; Liu *et al.*, 2007b). However, our numerical results show that the value of $\beta_{k,l,0}$ is in the same order of magnitude as that of $\alpha_{k,l,0}$. The overestimate of exciton-like interaction in our work originates from the following two reasons: (1) in the current expression for V_{xc} in Eq. (4.36), $\partial V_{xc}[\rho(z)]/\partial\rho(z)$ is proportional to $\rho(z)^{-2/3}$, which will lead to unreasonably large values of $\partial V_{xc}[\rho(z)]/\partial\rho(z)$ in barrier layers. (2) because of the low barrier height, in comparison with midinfrared QWIPs, more portions of the wave function will extend into the barrier layer. For the above two reasons, the integration value in Eq. (4.38) will be overestimated. The value of $\beta_{k,l,0}$ should be much smaller than that of $\alpha_{k,l,0}$ (Schneider and Liu, 2006). Therefore, for the present work, we leave out the exciton-like contribution.

In conclusion, we have investigated the effects of exchange-correlation, depolarization, and exciton-like interactions on the photon response spectra of THz QWPs. Because of the decrease of energy difference between the ground subband and the first excited subband, large relative errors are introduced without including the above many-body interactions in the theoretical design. The exchange-correlation potential deepens the quantum well. As a result, the ground subband and the first excited subband shift to the lower energy region, and the energy difference between them increases. Because the expression for exchange-correlation potential is inadequate in the low electron density region and the leakage of wave function into the barrier layer, the exciton-like interaction is overestimated. The discrepancy between the theoretical and experimental photoresponse peak positions decreases evidently by including the exchange-correlation and depolarization effects. Our numerical results show that it is very important to consider the many-body interactions for designing THz QWPs.

3.5. Simulation and optimization of grating coupler

The ISBT selection rule requires a nonzero polarization component in the quantum well direction (the epitaxial growth direction, z) (Schneider and Liu, 2006). As mentioned earlier, 45° incident, light-coupling geometry is usually used to acquire a nonzero polarization in z direction. However, this prevents the construction of two-dimensional (2D) focal plane arrays, which need light incident normal to the devices (the QW planes, xy plane). To solve this problem, it is useful to utilize gratings, as exploited by Heitmann *et al.* (1982) to diffract the light and thus excite ISBT in Si inversion layers. In the midinfrared region, large-format arrays with up to 1024×1024 pixels have already been demonstrated (Gunapala *et al.*, 2005). Recently, Patrashin *et al.* (2006) fabricated one-dimensional (1D) metal gratings on the top of the THz QWP, realizing device response under normal incidence (Patrashin and Hosako, 2008).

We utilized Modal method (Todorov and Minot, 2007) to simulate the field distribution in the 1D metal grating THz QWP (Zhang *et al.*, 2011). The average intensity in device active region was obtained. Based on numerical results, the optimizations of the grating including period and fill factor were discussed, which led to high coupling efficiency and device responsivity.

Usually, GaAs/AlGaAs material system is used to fabricate THz QWPs. The device is grown on semi-insulating (SI) GaAs substrate. From the bottom to the top, there are bottom contact, multiple quantum wells and top contact, shown in Fig. 4.8. The top and bottom contacts are n-doped GaAs, and the multiple quantum wells consist of several tens of AlGaAs barrier and n-doped GaAs well. The 1D metal grating is made of gold and is defined using standard mirofabrication lift-off techniques. The period of the grating is d, and the width of metal stripe is a.

The modal method is proposed by Todorov and Minot (2007). This method combines the Rayleigh expansion method of the diffracted field and the transfer matrix method of the multilayer, by which the electric field distribution in the device can be obtained conveniently.

The field appears in the form of a Rayleigh expansion in the homogeneous layers outside the 1D grating:

$$\psi(x,y,z) = e^{i\beta y} \sum_{n=-\infty}^{\infty} e^{i\alpha_n x} \left(P_n e^{i\gamma_n z} + Q_n e^{-i\gamma_n z} \right), \tag{4.39}$$

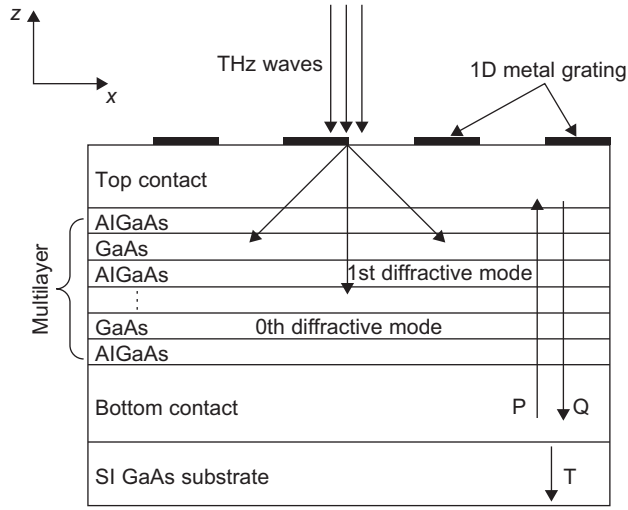

FIGURE 4.8 Schematic of 1D grating THz QWP (Zhang *et al.*, 2011).

$$\alpha_n = \alpha + \frac{2\pi n}{d}, \tag{4.40}$$

$$\gamma_n = \sqrt{\varepsilon k_0^2 - \alpha_n^2 - \beta^2}, \tag{4.41}$$

where ψ is any component of the field, ε is the dielectric function of the material, k_0 is the wave vector in the vacuum, and α_n is the wave vector in x direction. The x, y, and z direction are shown in Fig. 4.8. $\alpha_0 = \alpha$ is the wave vector of incident wave in x direction. The conservation of the tangential component of the wave vector at the grating surface leads to Eq. (4.40). β and γ_n are the wave vectors in y and z direction, respectively. (P_n,Q_n) is the pair of amplitudes (see Fig. 4.8), and all the pairs in different layers are connected with each other through transfer matrix. For the incident area outside the device, $Q_n = 0$ except Q_0, and $Q_0 = 1$ if the amplitude of incoming wave is set to be 1; while for the transmitted area, $P_n = 0$ and $Q_n = T_n$.

The field distribution can be obtained by solving the simultaneous equations in different areas with the boundary conditions. For normal incidence, only p polarization is need to be considered because no contribution is from s polarization which is in parallel with the QW planes makes no contribution. A typical field distribution (E_z component) in 1D metal grating THz QWP is shown in Fig. 4.9 (only E_z component contributes to the ISBT). Compared with the total thickness of the active region (less than 5 μm), the GaAs substrate is much thicker, normally around 600 μm, which is also much longer than the wavelength. So an approximation of infinite substrate is taken in the calculation for simplicity, which will not affect the diffractive characteristic of the grating.

In Fig. 4.9A and B, we can see a pair of stripes beneath the grating. This indicates the diffraction occurs and the nonzero E_z component appears, which will cause the response of the detector. The field distribution in the substrate is also given in Fig. 4.9. The periodic dark and light stripes are similar with the multislit interference. In the following, we will discuss the optimization of the 1D metal grating based on the E_z in the active region.

Two THz QWPs are considered here (Liu *et al.*, 2008). The multilayer is sandwiched between 0.4 and 0.8 μm of top and bottom contacts, doped to 1.0×10^{17}. The structures are detailed in Table 4.1. The optimization is discussed from the period d and the fill factor r (i.e., the ratio of metal stripe width a and d).

L_w is the quantum well width, L_b is the barrier width, N is the period number of multilayer, [Al] is the Al fraction in the barrier, N_d is the doping density in the well, and f_0 is the peak response frequency of the device.

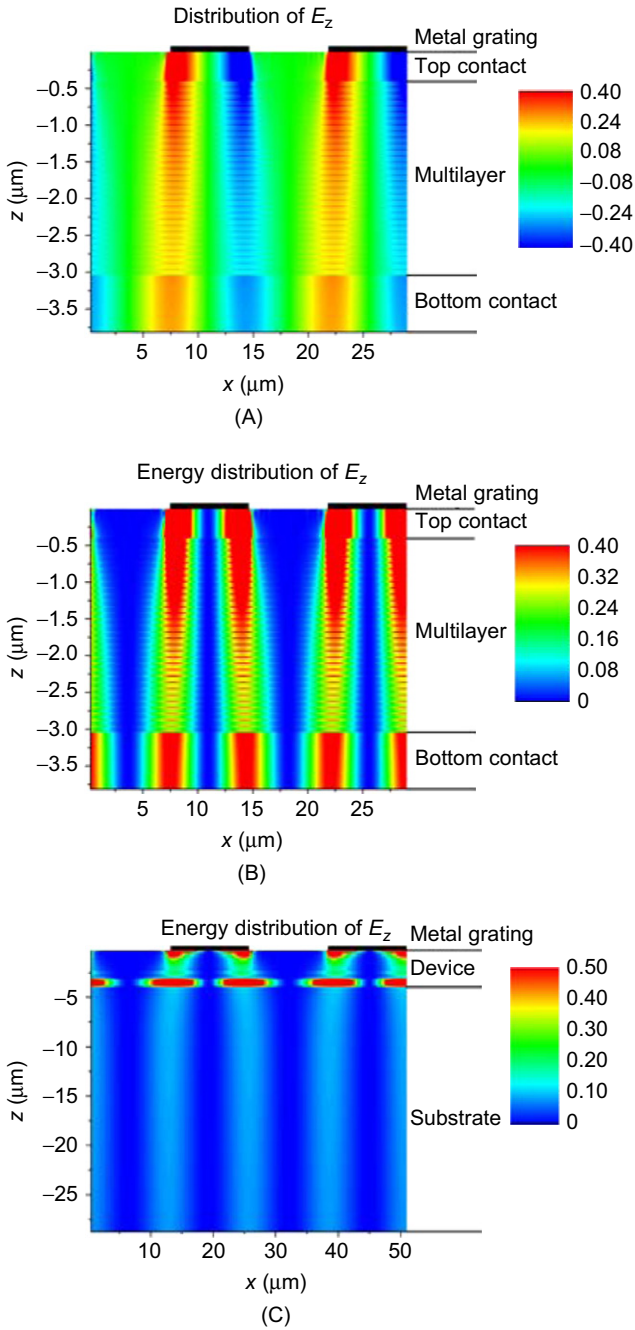

FIGURE 4.9 In a typical 1D metal grating THz QWP, (A) the distribution of E_z (amplitude); (B) the energy distribution of E_z (intensity), without the part of substrate; (C) the energy distribution of E_z (intensity), including the part of substrate. The metal grating is at $z = 0$, which is the top of the device (Zhang *et al.*, 2011).

TABLE 4.1 The structure parameters of THz QWPs

	L_W (Å)	L_b (Å)	N	[Al]	N_d (cm^{-3})	f_0 (THz)
A	155	702	30	3%	6×10^{16}	5.41
B	221	951	23	1.5%	3×10^{16}	3.21

The dielectric function is taken as follows (Blakemore, 1982):

$$\varepsilon(\omega) = \frac{\omega_{TO}^2 (\varepsilon_s - \varepsilon_\infty)}{\omega_{TO}^2 - \omega^2 - i\omega\delta_{TO}} + \varepsilon_\infty \left[1 - \frac{\omega_P^2}{\omega(\omega + i\delta_P)}\right] \tag{4.42}$$

For GaAs, $\varepsilon_s = 12.85$, $\varepsilon_\infty = 10.88$, $\omega_{TO} = 2\pi \times 8.02\,\text{THz}$, $\delta_{TO} = 2\pi \times 0.06\,\text{THz}$, δ_P is the damping rate, depending on the doping density N_P, Drude frequency ω_P is

$$\omega_P = \sqrt{\frac{N_P e^2}{\varepsilon_0 \varepsilon_s m*}}, \tag{4.43}$$

where e is the charge of electron, and m^* is the effective mass of free carriers.

The Drude model of metal is

$$\varepsilon_M(\omega) = 1 - \frac{\omega_M^2}{\omega(\omega + i\delta_M)} \tag{4.44}$$

For gold, $\omega_M = 1.11 \times 10^4\,\text{THz}$ and $\delta_M = 83.3\,\text{ps}^{-1}$.

The thickness of 1D metal grating studied here is 0.38 μm, deposited on the top of top contact. With these parameters, we calculate the average intensity $I_{average}$ of E_z in the active region at the peak response frequency f_0, which are 5.41 THz and 3.21 THz for device A and B, respectively. The expression of $I_{average}$ is

$$I_{average} = C\frac{\int \left|E_z e^{i\omega t}\right|^2 dV}{V} \tag{4.45}$$

where C is the constant of proportionality. It should be mentioned that, because of the much smaller thickness of metal grating than the width, most of the metallic losses are expected to occur along the walls parallel to the xy plane. The perfect-metal approximation is not suitable anymore, so we take the surface impedance boundary condition to take into account the dissipation in the metal (Todorov and Minot, 2007). Figure 4.10A gives the relation of $I_{average}$ and the grating period at 50% fill factor. It can be seen that the average intensities reach the maximum at 14.6 μm and 25.7 μm for A and

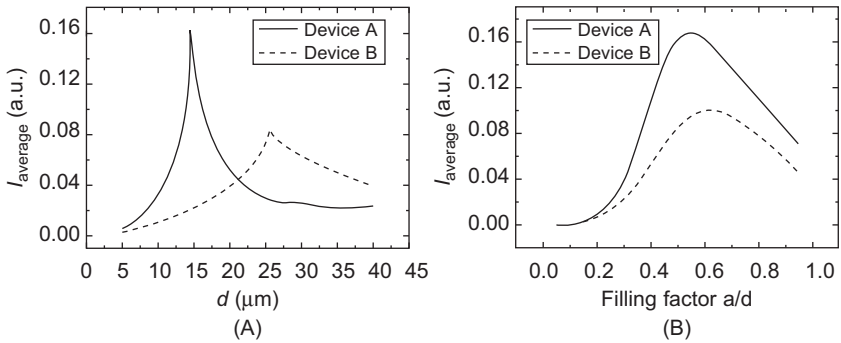

FIGURE 4.10 At peak response frequency (A) I_{average} versus the grating period under the condition of 50% fill factor; (B) I_{average} versus the fill factor when the period of grating is set to match the wavelength (Zhang *et al.*, 2011).

B, respectively, which correspond to the wavelength of THz waves at f_0 in the device material (in GaAs, 5.41 THz corresponds to 14.6 μm, and 3.21 THz corresponds to 25.7 μm). Therefore, when the period of the grating equals the wavelength in the device material, the coupling efficiency reaches the maximum. Then, we fix the grating period according to the peak response, and study the relation between average intensity and the fill factor. The results are given in Fig. 4.10B. For device A, the maximum occurs at 54.5% when the grating period is 14.6 μm; and for device B, it is 61.5% when the grating period is 25.7 μm. The results are not 50%, which may be related to the transmission and reflection of the multilayer. So the fill factor should be determined according to the specific structure of a THz QWP.

To confirm these predictions, we fabricated three grating samples (A-G12 with a 12-μm-period grating, A-G15 with a 15-μm-period grating, and A-G20 with a 20-μm-period grating). At 0.15-V bias, the peak responsivities are 0.128, 0.197, and 0.070 A/W for A-G12, A-G15, and A-G20, respectively. It can be seen that, the 15-μm-period grating is the most efficient one, which is in consistent with our prediction.

In conclusion, the Modal method is used to analyze the electric field distribution in the 1D metal grating THz QWP, and the optimization of the grating is also discussed based on the simulation. We find that, when the period of the grating equals the wavelength in the material and a proper fill factor is chosen (54.5% for A device, 61.5% for B device), the coupling efficiency reaches a maximum, leading to high field intensity and high detector's responsivity. Moreover, we find that the thickness of substrate is important for the field distribution, which may be caused by the cavity effect. Further investigation is needed.

4. DESIGN AND CHARACTERIZATION OF THz QWP

4.1. Design

The detection of THz waves is the one of the key technology of THz applications. To study the THz wave itself and its interaction with other materials, various characterizations should be done, including spectrum measurement, power calibration, beam analysis, and so on. Because of the specific position in the electromagnetic wave spectrum, the study of THz range developed slowly for a long time because of the lack of radiation sources and detectors, and hence limited the methods that could be used for detection. In the recent 10 years, as the development of compact THz sources and the detection methods, the methods for detection of THz waves improved substantially (Tonouchi, 2007). Therefore, different sources and detectors could be chosen, and various physical phenomena could be studied.

THz QWP is the extension of QWIP in THz range. The materials are commonly GaAs/AlGaAs. The optimum QW parameter for a standard QWIP is to have the first excited state in resonance with the top of the barrier. Strong ISBT absorption and fast relaxation of excited electrons can be both achieved in this structure. Therefore, the structure parameters should be optimized in design. These strcture parameters are the quantum well width, barrier width, doping density, barrier height (the Al fraction in AlGaAs barrier), and the number of quantum wells. For THz QWP working at longer wavelength than QWIP, smaller barrier height and lower doping density are required (to reduce the absorption by free carriers and the dark current).

In 2004, Liu *et al.* (2004) demonstrated the first THz QWP with a peak response at 7.1 THz (42 μm). The width of quantum well and barrier are 12 nm and 40 nm, respectively. The Al fraction is 5%, and the number of quantum wells is 50. The center 10 nm of the quantum well and the top (400 nm) and bottom (700 nm) GaAs contacts are doped to 10^{17} cm^{-3} by Si.

The calculated parameters of barrier Al percentage and well width for a given peak detection frequency (wavelength) are shown in Fig. 4.11 (Liu *et al.*, 2004). A word of caution: the parameters used here, although expected to be valid, are proven for midinfrared QWIPs and are not tested in the low aluminum fraction region. From Fig. 4.11, it is predicted that the THz frequency range of 1–8 THz is covered by QWIPs with low aluminum fractions between 0.8 and 5.4%.

Figure 4.12 shows the calculated T_{blip} versus the peak detection frequency (Liu *et al.*, 2004). For achieving the highest dark-current-limited detectivity, if one follows the $E_f = 2k_BT$ rule, the density would become very low for low temperatures ($\ll$80 K), making the absorption also low.

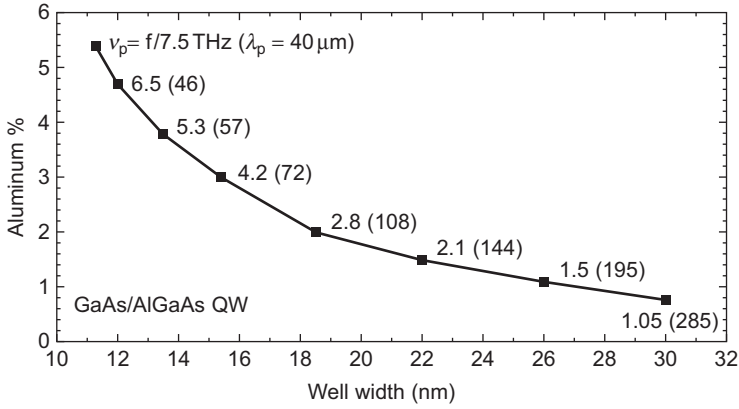

FIGURE 4.11 Calculated parameters of barrier Al percentage and well width for a given peak detection frequency (wavelength) (Liu *et al.*, 2004).

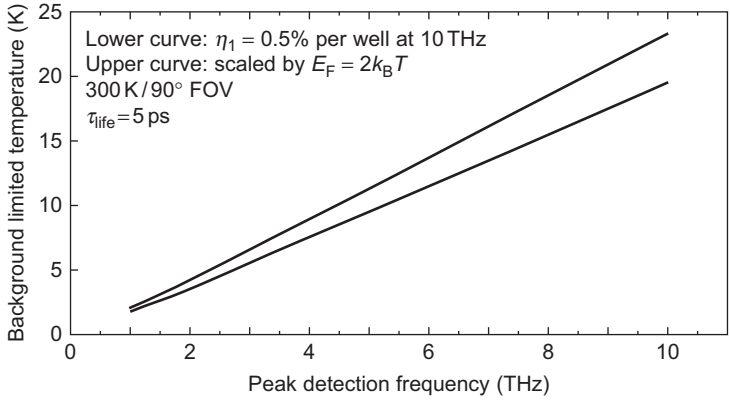

FIGURE 4.12 Calculated background-limited infrared performance (blip) temperature versus peak detection frequency (Liu *et al.*, 2004).

We, therefore, considered two cases in Fig. 4.12. The upper curve uses the $E_f = 2k_BT$ condition, while the lower curve starts with a higher absorption (using higher doping) 0.5% at 10 THz and is reduced linearly down to 0.05% at 1 THz. The trade-off here is that if the operating temperature is desired to be as high as possible, the upper curve should be followed. However, if a high absorption is needed, one should use the lower curve, which will mean a somewhat lower operation temperature. Because for these very far-infrared devices the doping densities are usually low, many-body effects result in small energy corrections. However, because of the transition energies are also small, many-body effects need to be considered. The exact

values depend on doping densities. The detection frequency in Fig. 4.12 should, therefore, be shifted to higher values by about 30% if these effects are included. In general, to qualify as a good detector, there must be a sufficiently high absorption. On one hand, a high doping is desirable for achieving high absorption; but on the other hand, high doping leads to a high dark current and low operating temperature. A trade-off must, therefore, be made for a given application. For most applications, it is desirable to operate the detector under the blip condition for detecting weak signals. In some applications involving a strong source such as a THz QCL, the requirement is different. Here as long as the dark current is lower than the signal photocurrent, photon noise limited detection is achieved. In such a case, the detector operating temperature can be raised.

Having determined the quantum well and doping parameters, the next design parameter is the barrier width. The barrier width should be sufficiently thick so that the dark current is completely in the thermionic regime, i.e., interwell tunneling should be negligible comparing to the background photocurrent. The barrier thickness was chosen according to Fig. 4.13 so that the interwell tunneling currents are less than 10^{-5} A/cm^2, which corresponds to the estimated background current.

For the number of quantum wells, because the absorption strongly depend on the device geometry and the coupling method, generally a large number of wells would give a high absorption. However, provided

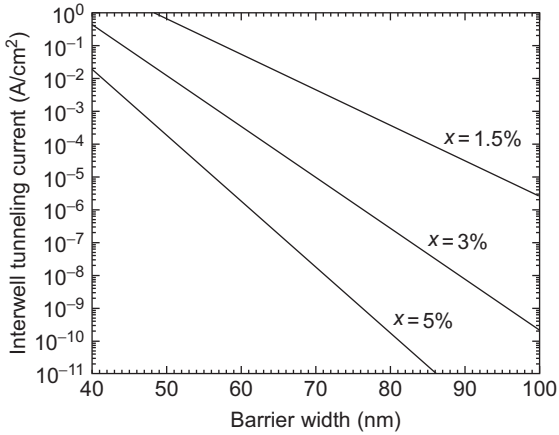

FIGURE 4.13 Estimated direct interwell tunneling current versus barrier thickness for three cases of barrier aluminum fractions of $x = 1.5$, 3, and 5%. Other parameters used for the estimate are $E_1 = 4.3$, 8.6, and 14 meV, $n_{2D} = 0.3$, 0.6, and 1.0×10^{11} cm^{-2}, and $L_W = 22.0$, 15.4, and 12.0 nm, for the three x values, respectively (Schneider and Liu, 2006).

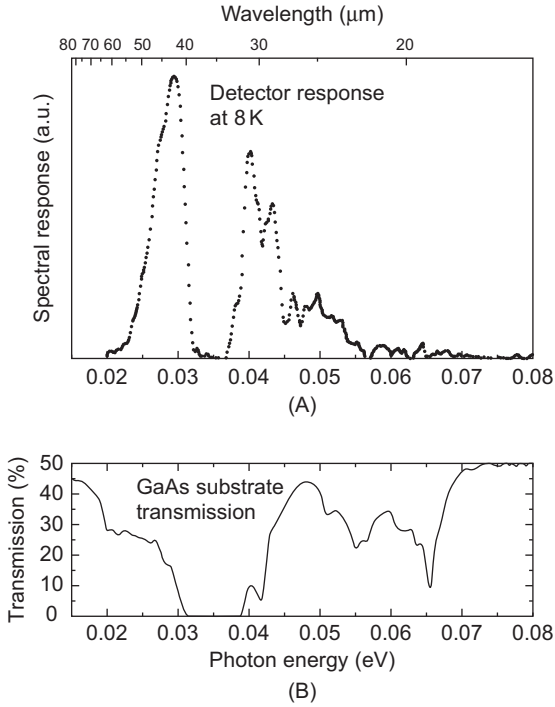

FIGURE 4.14 (A) Photoresponse spectrum and (B) low temperature bulk GaAs transmission spectrum (Liu *et al.*, 2004).

a sufficient absorption is reached, a small number of wells is preferred for high gain.

The photoresponse spectrum is shown in the upper part of Fig. 4.14 (Liu *et al.*, 2004) for a bias voltage of 0.4 V and a temperature of 8 K. For reference, the bulk GaAs transmission is shown in the lower part of the figure, measured at 15 K on a 400-mm-thick GaAs substrate. The "dark" reststrahlen region from 33 to 37 meV resulting from optical phonon absorption is clearly seen. We simulated the photocurrent spectrum (Cao *et al.*, 2006) theoretically by the improved photo response model, which is in consistent with the experimental data above. As a result of the interaction between electron and phonon, the radiation with frequency in the "dark" region cannot be detected by GaAs/AlGaAs THz QWPs. The measured dark current characteristics at various temperatures are shown in Fig. 4.15 (Liu *et al.*, 2004). The measured dark current slowly decreased to less than 25 K and stopped at about 15 K. These studies confirm that the structure of QWPs is practicable in THz detection.

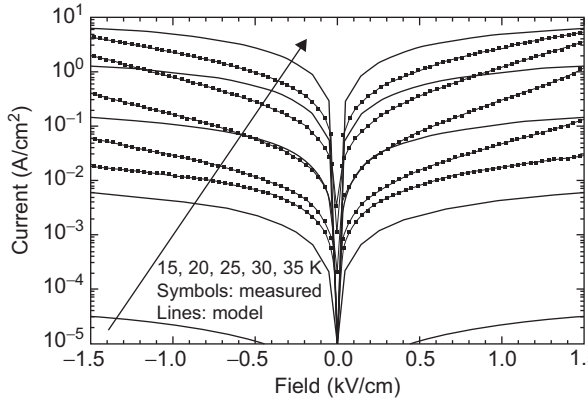

FIGURE 4.15 Dark current characteristics at various temperatures (Liu *et al.*, 2004).

In addition, Graf *et al.* (2004) demonstrated a THz quantum well photodetector based on the quantum cascade structure, with the peak response wavelength of 84 μm (3.57 THz), operating at 10–50 K. The responsivity at 10 K is 8.6 mA/w. Although the detectivity and the responsivity are two orders of magnitude smaller than the THz QWP based on photoemission, its noise level is relative low because of the cascade mechanism. Because of the potential of zero bias photovoltaic response, the development of this type of detectors is also very interesting.

4.2. Measurement of photocurrent spectrum

Terahertz radiation bridges the gap between the microwave and optical regimes. It is only 5 years since the first demonstration of THz QWP (Liu *et al.*, 2004), and a lot of researches are still needed. Before the measurement of photocurrent spectrum, we test the I–V curves first, then analyze the dark current mechanism and the temperature performance.

The temperature-dependent I–V properties are important characteristics for terahertz QWPs. In the following, we measured the I–V curves with 300 K background or the dark condition, and the relation between dark current and temperature is also discussed. The active region of the device is GaAs/AlGaAs multiquantum wells grown by MBE. The parameters of the active region are shown in Table 4.2. It should be mentioned that the doping in Table 4.2 is implemented at the center 10 nm of the quantum well by Si. The purpose of the wide barriers is to reduce the interwell tunneling (Liu *et al.*, 2007a). In a real device, the active region is between the top and bottom contacts. The top and bottom contacts are usually 400 and 800 nm respectively, doped to 1×10^{17} cm^{-3} with Si, which is relatively low

TABLE 4.2 Structure parameters for the THz QWIPs (Schneider and Liu, 2006)

Sample	L_w (nm)	L_b (nm)	[Al]	N_d (cm^{-3})	N
V265	11.9	55.2	0.05	1×10^{17}	40
V267	22.1	95.1	0.015	3×10^{16}	23

to reduce the contact layer free carrier absorption and plasma reflection in the THz region (Schneider and Liu, 2006). Next, we will mainly introduce the measurement and analysis of V267.

Mesa devices of different sizes were fabricated using standard GaAs processing techniques. Because low temperatures are required for operation, a close-cycle cryostat with the lowest temperature of 3 K is used to cool the device. A source meter is used to provide the external bias, and the current is also recorded at the same time. The bias range is from 1 to 30 mV during the measurement.

The current–voltage curves under dark condition (solid) and under a 90° FOV 300-K background (dash) at the temperatures from 3.15 to 20 K are shown in Fig. 4.16. Because thermionic emission and field-assisted tunneling were much stronger than interwell tunneling within the experiment temperature range, we did not observe any current bottom-out behavior (Schneider and Liu, 2006). As in Section 2. Tblip is a good figure-of-merit of a detector. The measured T_{blip} of V267 is 12 K. Sequential tunneling and thermionic emission are two major dark current mechanisms in GaAs/AlGaAs barrier structures (Levine, 1993), and the latter becomes dominant for thick barrier structures. From the I–V curves in Fig. 4.16A, the I–T curves have been obtained and shown in Fig. 4.16B. The dark current decreased by six to seven orders of magnitude in accordance with the thermally activated character of the thermionic emission (Çelik *et al.*, 2008) when the device was cooled from 20 K down to 3.15 K, which indicates that the use of the emission-capture model, combined with the 3D carrier drift model, is reasonable for describing the dark current of this detector. A steep drop of the I–T curves when the device temperature $\leq$12 K has been observed, which is consistent with the good performance when the device is operating at and lower than T_{blip}. Next, we will introduce the measurement and analysis the photocurrent spectra of 2 THz QWPs (V265 and V267).

The measured photocurrent spectra of V267 at different bias voltages are given in Fig. 4.17A. The operating temperature is 3.15 K. The peak response is 3.2 THz, corresponding to 93.6-μm wavelength. Strong response also exists in the range from 3 to 5.3 THz, which can be used to characterize the THz radiation source in this region. In addition, the photocurrent spectra at different operating temperatures under 30-mV bias are also measured, see Fig. 4.17B. Upon increasing of the operating temperature, the photocurrent

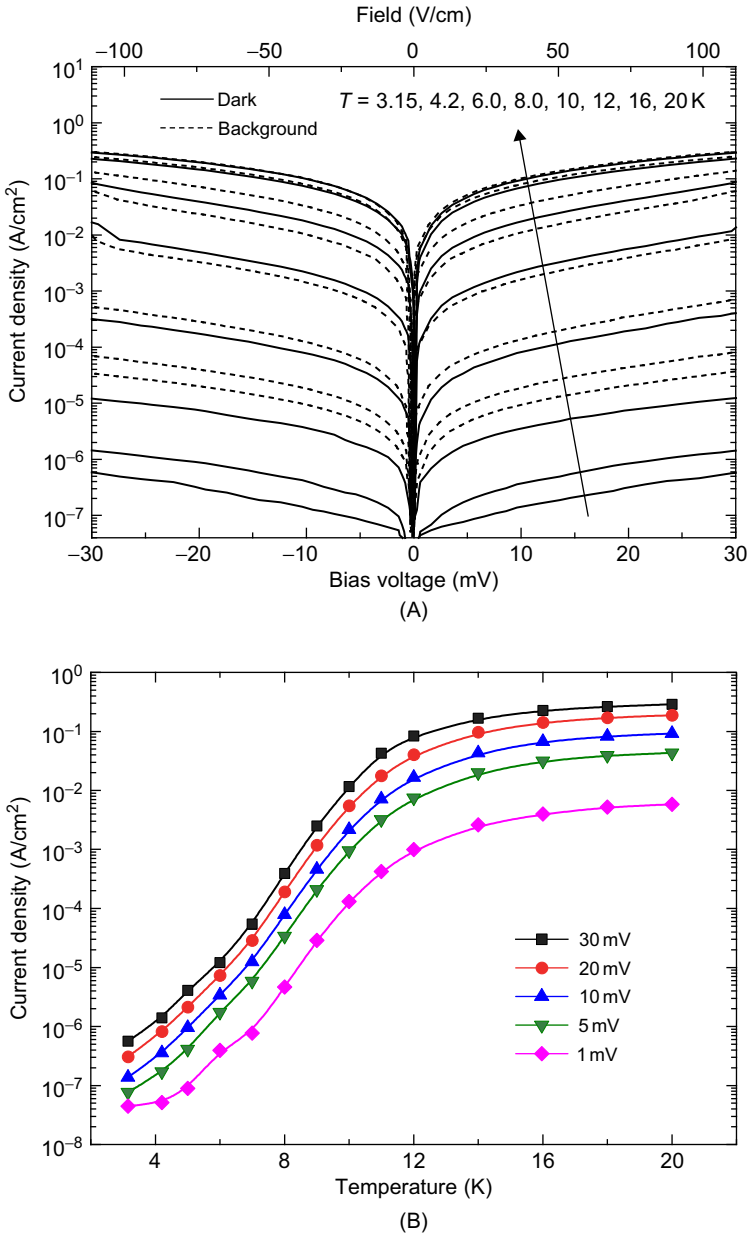

FIGURE 4.16 (A) Current–voltage curves of V267 under dark condition (solid) and under a 90° FOV 300-K background (dash) at different temperatures; (B) Current–temperature characteristic measured at selected bias voltages.

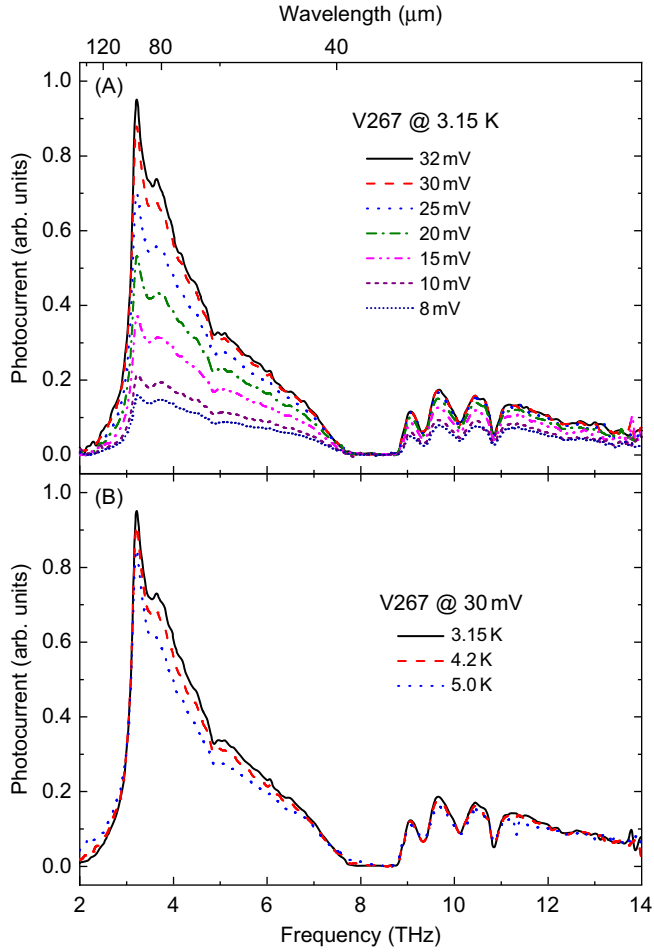

FIGURE 4.17 Photocurrent spectra of V267 at (A) different bias voltages and (B) different operating temperatures.

response decreases. The shape of the spectra doesn't change significantly because of the small temperature range of the measurement.

Photocurrent spectra of V265 at different bias voltages at 3.5 K are shown in Fig. 4.18. It can be seen that the peak response is 9.7 THz (wavelength of 31.0 μm). The theoretical peak response is around 7 THz for the structure of V265. The differences are caused by the phonon absorption of GaAs, leading to a dark region from 32 to 37 meV. Stronger photocurrent could be generated with higher bias, so the amplitude of photocurrent spectrum increases when the external bias is increased.

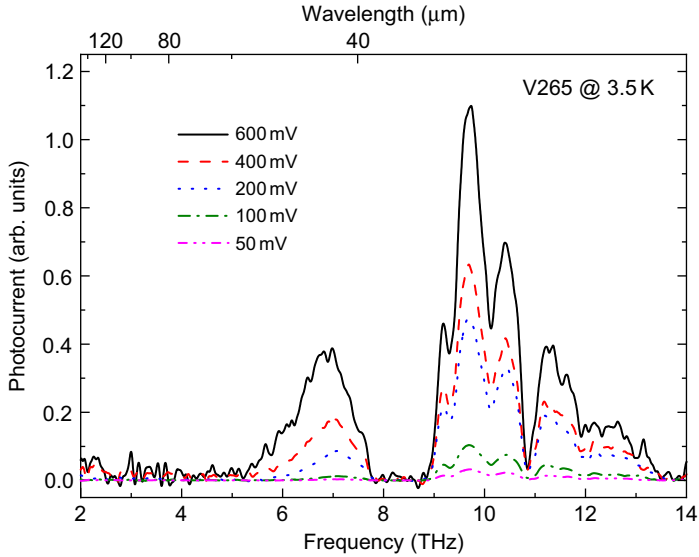

FIGURE 4.18 Photocurrent spectra of V265 at different bias voltages at 3.5 K.

4.3. THz QCL emission spectrum measured by THz QWP

We use a THz QWP to characterize the emission spectrum of a THz QCL (Tan *et al.*, 2010). The shape and peak of the emission spectrum are acquired, and the relation of the emission power with driving current is estimated, from which the current density range of lasing and the threshold are obtained. The detection performance of THz waves from the THz QCL by THz QWP is also studied at different temperatures. We found that THz QWP is a good detector in characterizing the emission spectrum of THz QCL. The emission spectrum is an important characterization of a laser. Usually to measure the emission spectrum of a THz QCL, a Fourier Transform Spectrometer is used. To reduce the absorption by the water vapor, the spectrometer should be evacuated. A bolometer operating at the liquid helium temperature is often used to measure weak signal. In this section, we will mainly introduce the measurement of the emission spectrum of a continuously THz QCL by a Fourier Transform Far-Infrared Spectrometer operating at linear scan mode.

The structure of the active region of the THz QCL is given in the study by Li *et al.* (2009b), and the sample ID is B1316 PKG3. Because low temperature is required for the laser operation, we use a close-cycle cryostat to cool the laser. The lowest temperature is 9 K. The radiation of the THz QCL enters the FTIR through the windows of the cryostat and the spectrometer. The scan

speed and the resolution of the FTIR are set to be 1.6 KHz and 0.25 cm^{-1}, respectively. The beam splitter is 6 μm Mylar, and the detector is DTGS-PE. The range of wave number is 100–160 cm^{-1}, and the THz QCL is driven by a DC bias at 10 K. We measured the emission spectra of the THz QCL at different driving currents and operation temperatures.

THz QCL and THz QWP are both multiquantum well devices. Hosako *et al.* (2007) suggested that THz QWP could be used to detect the emission of THz QCL. In the following, we will use a THz QWP to characterize the emission spectrum of a THz QCL.

Before the characterization of THz QCL using THz QWP, we discuss the feasibility from the spectra (Tan *et al.*, 2010). The photocurrent spectrum of the THz QWP at 3.15 K under the illumination of a Globar is shown in Fig. 4.19. In order to compare with the emission spectrum of the THz QCL, the photocurrent signal is normalized, the inset shows the same spectra on an expanded range. It can be seen that the response peak of the THz QWP is 3.2 THz. The response at 4.13 THz is about 67% of the peak, and strong response occurs in the range of 3–5.3 THz

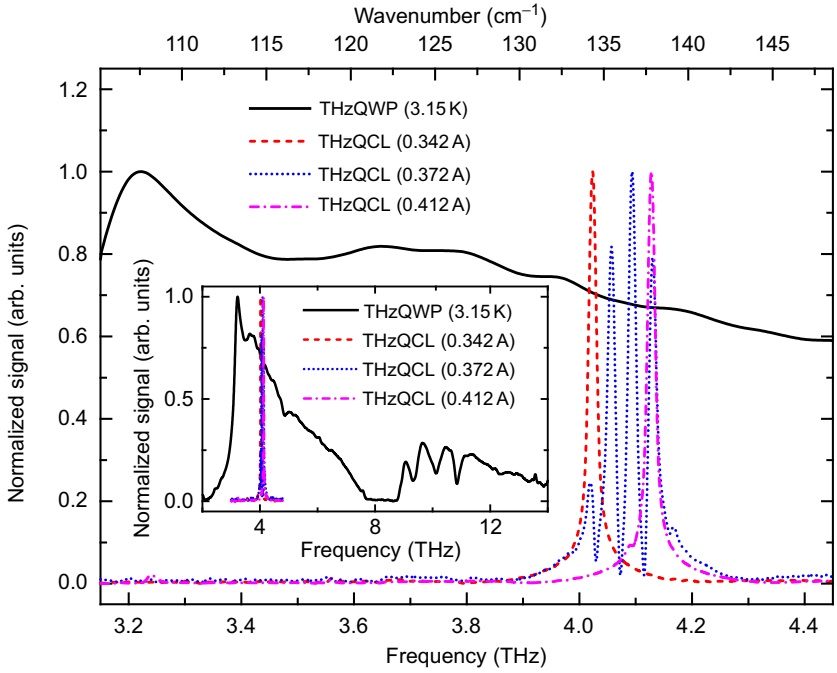

FIGURE 4.19 Comparison of the photocurrent spectrum of the THz QWP and the emission spectrum of the THz QCL. The operation temperatures are 3.15 and 10 K for THz QWP and THz QCL, respectively (Tan *et al.*, 2010).

(normalized amplitude ≥40%). The four emission peaks of the THz QCL are 4.022 THz (134.27 cm^{-1}), 4.058 THz (135.48 cm^{-1}), 4.094 THz (136.68 cm^{-1}), and 4.130 THz (137.89 cm^{-1}). The emission peaks are all in the region in which the curve of the response of the THz QWP is relatively flat. Moreover, the responsivity of the THz QWP is about 0.4 A/W (Luo *et al.*, 2005), which is comparable with the mid-infrared QWIP with similar structures (Levine, 1993). Therefore, the characterization of THz QCL with THz QWP is practicable.

The characterization by THz QWP is similar to that by DTGS-PE. We simply replace the DTGS-PE with the THz QWP as the FTIR system detector.

The I–V curve and the L–I curve of the THz QCL are shown in Fig. 4.20 (Tan *et al.*, 2010). It can be seen that the current density range of lasing and the threshold are the same as those measured by the DTGS-PE. The threshold is 630 A/cm^2. The main differences of the L–I curves are because of the electrical noise. The area marked by pattern is the multipeak operating region. The results indicate that the performance of the THz QWP in characterizing the emission spectrum of the THz QCL is comparable with the DTGS-PE. Improvements could be done on reducing the electrical noise.

The emission spectra of THz QCL working at different driving current are shown in Fig. 4.21, where the solid line and the dashed line correspond

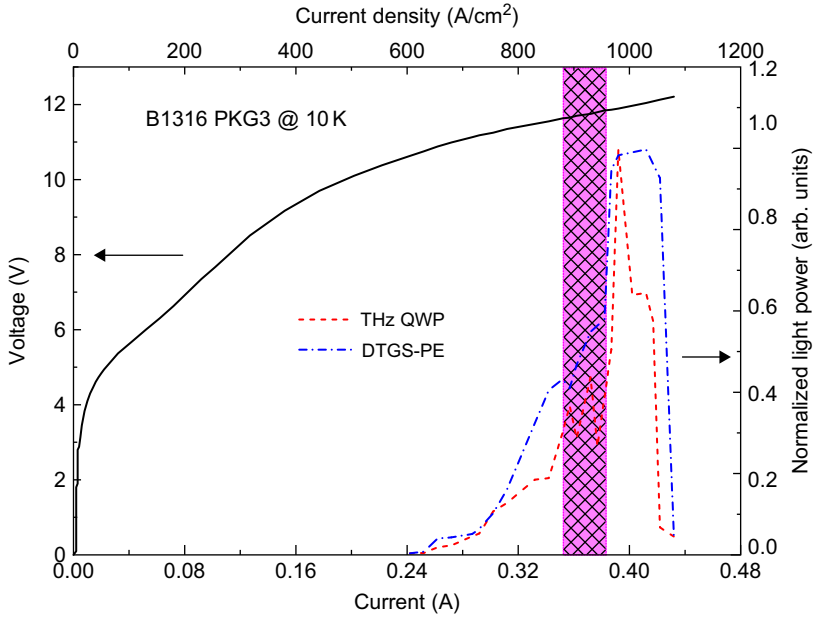

FIGURE 4.20 The I–V curve (solid line) of the THz QCL and the P–I curves from THz QWP (dashed line) and DTGS-PE (dash-dot line), respectively (Tan *et al.*, 2010).

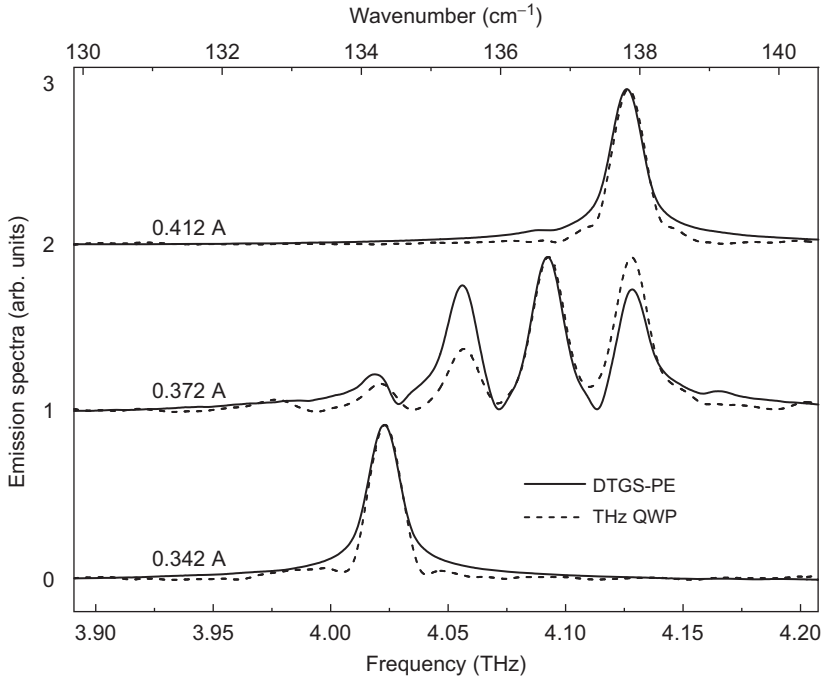

FIGURE 4.21 The emission spectra of the THz QCL taken by the THz QWP (dashed line) and the DTGS-PE (solid line) (Tan *et al.*, 2010).

to measurements taken by DTGS-PE and THz QWP, respectively. The spectra are normalized and shifted in vertical axis for clarity. The spectrum in dashed line is sharper than the one in solid line. The difference may be from the artifact caused by the difference in preamplifiers and circuits. The multipeaks and the blue shifts by the Stark effect are seen by both detectors (Bastard *et al.*, 1982; Williams *et al.*, 2003).

The results above show that THz QWP is good at characterizing the performance of THz QCL, and its high-speed response is much superior to traditional detectors. The measurements above establish the basis of wireless communication based on THz QCLs and THz QWPs and the time-resolved spectrum applications.

5. APPLICATION: THz FREE SPACE COMMUNICATION

It is anticipated that many new applications in the THz spectrum are possible if simple compact sources and detectors were readily available. Many groups around the world are in the process of developing semiconductor

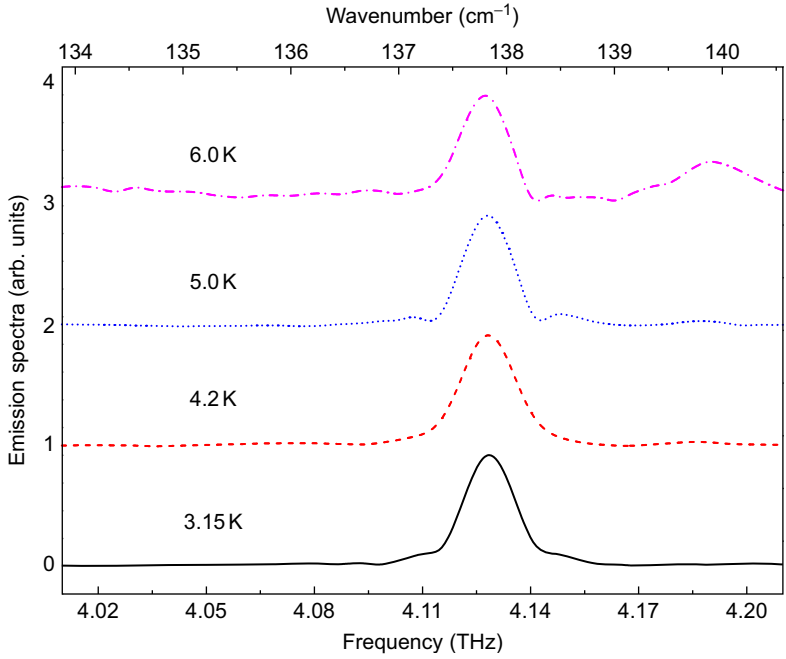

FIGURE 4.22 The emission spectra of the THz QCL taken by the THz QWP working at different temperatures (Tan *et al.*, 2010).

sources and photodetectors for the THz spectrum (Belkin *et al.*, 2008; Kumar *et al.*, 2009; Liu *et al.*, 2008; Scalari *et al.*, 2009). A demonstration of a sub-THz analog transmission system was reported by Jastrow *et al.* (2008) at 300 GHz using an electronic system. In this section, we present a demonstration of an all photonic terahertz communication link operating at 3.8 THz using a quantum cascade laser and quantum well photodetector (Grant *et al.*, 2009). The link consists of a quantum cascade laser transmitter and a quantum well photodetector receiver. The link was used to transmit audio frequency signal through 2 m of room air. Carrier strength at the photodetector was 100 times greater than the noise level.

Figure 4.23 is a schematic representation of the link. At the left, a quantum cascade laser housed in a vacuum dewar provides 3.8-THz radiation, which is collected and collimated by a parabolic mirror labelled M1. The laser transmitter was constructed from a multiple quantum well structure described earlier (Luo *et al.*, 2007) with a 1-mm-long and 100-μm-wide surface plasmon waveguide formed on a semi-insulating GaAs substrate. A reflecting mirror was formed on the back facet by first coating the facet with an aluminium oxide insulator, to prevent short circuiting the electrodes,

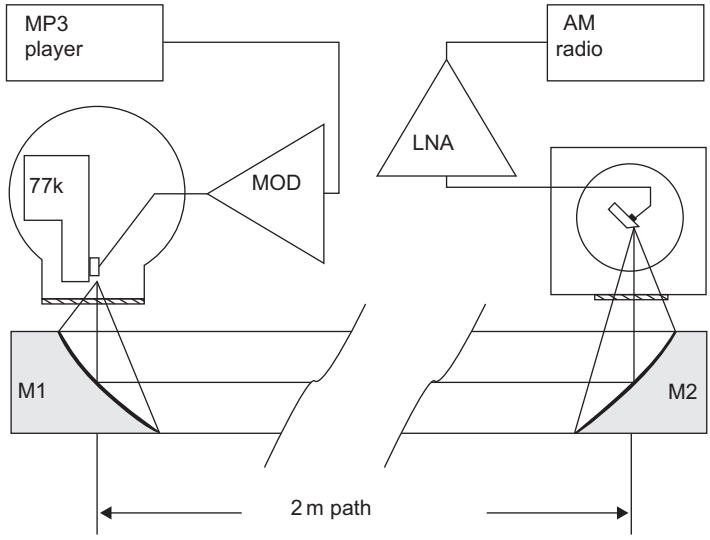

FIGURE 4.23 Schematic of link showing quantum cascade laser at left and quantum well photodetector on right (Grant *et al.*, 2009).

followed by evaporating a gold layer over the facet. The exit coupler of the laser is the cleaved surface. M1 is a 50-mm focal length off-axis parabolic reflector, whereas M2 is 76-mm focal length. Both mirrors are 50 mm in diameter. The laser was mounted on an aluminum cold finger in a liquid nitrogen dewar with the laser facet approximately 2 mm from the low-density polyethylene window. This permitted collecting a large fraction of the diverging beam with an off-axis parabolic mirror. A temperature sensor was mounted near the base of the QCL die and showed that the base temperature was maintained at 78 or 77 K.

Care was required to align the four optical components, the QCL, the QWIP, and the two mirrors. The initial alignment was performed in air without the polyethylene windows. The photodetector was displaced by 2 mm using a translation stage and a visible laser beam was passed through the photodetector location to the two mirrors and then to the laser. Crude alignment was performed to ensure that the laser was near the focus of each mirror and that the visible light was arriving at the QCL facet. The optical coupling was quite sensitive to the position of the QCL which was rather small. Sometimes, no coupling could be established after an optical component was moved, and we used a piece of 50-mm diameter Plexiglass pipe 200 cm long as a light guide. The QCL could then be focused on the end of the light pipe, which was only 10 cm away from the mirror. After a signal was established, the light guide could be removed, and there was

still sufficient signal to allow optimizing alignment of the long path. The position of the larger QW detector was not as critical.

A custom-made electronic pulse generator was fabricated to provide low-duty cycle pulses of amplitude V_H. The maximum V_H required was 17 V at a current of 2.6 A for a peak power of 43 W. The pulse width above threshold was approximately 8 ns. Pulse repetition frequency was 455 kHz. Total power injected was calculated from the recorded voltage waveform and integrated to give an average power of 0.16 W or a peak-to-average ratio of 268 : 1. The generator contained power amplifiers that forced V_H to follow the modulation voltage which we wanted to transmit, typically a sine wave at 500 Hz or music. The optimum conditions for V_H and modulation amplitude (V_M) were found by transmitting a 455-kHz carrier modulated by a 500-Hz sine wave while measuring the second harmonic at 1 kHz. Clipping by modulating less than threshold or more than saturation rapidly increased the second-harmonic content of the detected signal. It was found that the best V_M was about 1 V peak-to-peak with V_H of 15 V.

Numerical calculation of the Fourier transform of the expected photocurrent indicated that there should be a DC term, a modulation term, and a large number of replications of the pulse repetition frequency. Each replication would have a carrier plus modulation side-bands. The DC term is proportional to the average laser power and for the low-duty cycle pulses that we are using, the carrier amplitudes are equal to each other and to the DC term. This is a central point in the demonstration. Even though the laser was pulsed, the Fourier transform of the photocurrent contains useful continuous-wave (CW) components with amplitude equal to the average photocurrent. Further, the modulation side-bands contain the Fourier transform of the time variations of V_M.

Experimentally, the 500-Hz basic modulation term could be easily detected using a bolometer and lock-in amplifier. The 455-kHz pulse repetition frequency was also easily detected using the QWIP and could be observed on a spectrum analyzer as a typical amplitude modulated waveform. Figure 4.24 shows a typical nonmodulated spectrum measured at the pulse repetition frequency after the transimpedance amplifier. The left inset in Fig. 4.24 is an expanded spectrum of the laser measured using an Fourier transform infrared (FTIR) spectrometer. Both were measured while the QCL was being pulsed at 455 kHz with no modulation. Although none of the modulation can be resolved using the FTIR, the central emission line width is at the FTIR resolution of 0.04 wavenumbers or 1.2 GHz. The right inset shows the QW photodetector spectral responsivity overlaid with the 126 wavenumber laser spectrum at the left. The RMS photocurrent at the 455 kHz is two orders of magnitude greater than the noise level. The noise level from 450 to 460 kHz originates in the custom-made laser driver electronics and is not a fundamental limitation of the devices. Finally, the

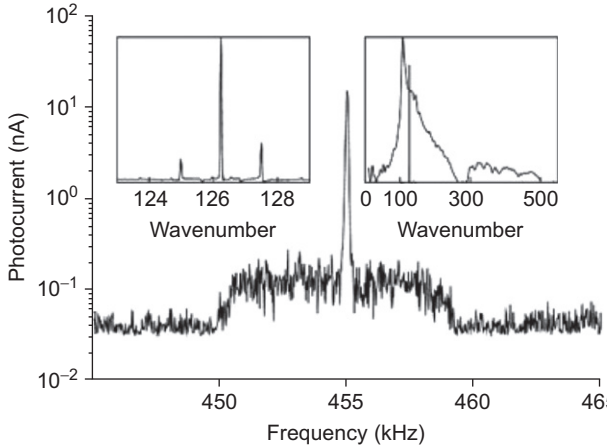

FIGURE 4.24 Spectrum of photocurrent measured after low-noise amplifier with insets showing laser spectrum at left and photodetector responsivity at right. Photodetector spectrum measured at temperature of 12 K (Grant *et al.*, 2009).

signal could be coupled to the antenna input of an AM radio (Sony ICF 2010) and music recovered.

The low-noise amplifier (LNA) has a transimpedance amplifier, a filter, and a buffer amplifier, as well as the photodetector bias circuit. The capacitance of the cable from the cold section to room temperature was measured as 160 pF plus the large QW photodetector capacitance of 88 pF caused instability in high-speed amplifiers that we initially tried to use. A general purpose operational amplifier with a 12-MHz gain bandwidth product could be made stable in a 1-kΩ transimpedance configuration. This was followed by a 455-kHz center frequency, 10-kHz bandwidth filter, and a line driver amplifier to provide an effective transimpedance of 10 kΩ. Detector bias was introduced at the input of the transimpedance amplifier. Typically, our measurements were performed with −20 mV of bias and 2 μA of total photodetector current. DC photocurrent was always less than 0.1 mA, the resolution of the meter, which was used for monitoring bias current. Using the QW detector responsivity measured in (Luo *et al.*, 2005) of 1 A/W and the property of the Fourier transform of a narrow pulse (with its low harmonics having the same amplitude as the average), the average optical power can be determined. The recovered 455-kHz carrier current was 18 nA RMS from which we calculate the average optical power to be $1.414 \times 18 = 25$ nW.

Although there are many atmospheric absorption bands known in the THz frequency region, we observed very little impairment of our link owing to atmospheric absorption. The center frequency of the laser was

3787 GHz as determined by FTIR measurement of the emission. Empirically, we measured the air in our laboratory in Ottawa, Canada, and observed that this frequency is at the upper edge of an essentially transparent region of the electromagnetic spectrum that extends from 3700 to 3789 GHz. This band is 89 GHz wide and is only one of many which we observe to be essentially transparent in room air. We point out that while there are many absorption bands because of water vapor, as much as 50% of the spectrum space we observe is transparent or of low absorption. We used a 50-mm diameter Plexiglass pipe as a gas cell and compared transmission through room air with transmission through dry nitrogen and found no difference. The only strong absorber that we observed was liquid water.

6. SUMMARY

We have introduced the principle, simulation and design method, and device performance of THz QWPs. At the present time, various incoherent detection methods (such as bolometer) and several coherent detection methods (such as THz TDS) are well developed and are used in spectroscopy and imaging fields. Because of easy production of high quality and large area uniform THz QWP materials, THz QWPs have great advantages in high sensitivity and high resolution detection, especially in the construction of focal plane arrays. THz QWPs are also useful in the detection of toxic materials and THz wireless communication. Because the characteristic absorption lines of most molecules are in THz range, under a normal continuous light source (such as high-voltage mercury lamp), monitoring of toxic materials can be achieved by THz QWPs because of their high spectrum resolution and high response speed. The monitoring ability can be improved by multicolor THz QWPs, and multiple identifications at the same time can also be achieved. It can be expected that the development of high-performance, single-element detectors and focal plane arrays will enable the THz communication and THz detection applications.

ACKNOWLEDGMENTS

We thank our colleagues and coworkers for their contributions, especially R. Zhang, Z. Y. Tan, X. G. Guo, Y. L. Chen, and F. Xiong in SIMIT, and M. Buchanan, R. Dudek, E. Dupont, M. Graf, P. D. Grant, H. Luo, A. J. SpringThorpe, C. Y. Song, and Z. R. Wasilewski of National Research Council Canada.

REFERENCES

Ando, T., Fowler, A. B., and Stern, F. (1982). *Rev. Mod. Phys.* **54**, 437.
Bastard, G., Mendez, E. E., Chang, L. L., and Esaki, L. (1982). *Phys. Rev. B* **28**, 3241.
Beck, W. A. (1993). *Appl. Phys. Lett.* **63**, 3589.

Belkin, M. A., Fan, J. A., Hormoz, S., Capasso, F., Khanna, S. P., Lachab, M., Davies, A. G., and Linfield, H. (2008). *Opt. Express* **16**, 3242.
Blakemore, J. S. (1982). *J. Appl. Phys.* **53**, R123.
Byer, N. E., Stokowski, S. E., and Venables, J. D. (1975). *Appl. Phys. Lett.* **27**, 639.
Cao, J. C. (2006). *Physics* **35**, 953.
Cao, J. C., Chen, Y. L., and Liu, H. C. (2006). *Superlattices Microstruct.* **40**, 119.
Çelik, H., Cankurtaran, M., and Altunöz, S. (2008). *Superlattices and Microstruct.* **44**(2), 237.
Cellek, O. O., and Besikci, C. (2004). *Semicond. Sci. Technol.* **19**, 183.
Cellek, O. O., Memis, S., Bostanci, U., Ozer, S., and Besikci, C. (2004). *Physica E* **24**, 318.
Chen, R. T., Rana, V., and Spitzer, W. G. (1980). *J. Appl. Phys.* **51**, 1532.
Chen, Y. L., Guo, X. G., and Cao, J. C. (2006). *Chin. Phys. Lett.* **23**, 1615.
Downey, P. M., Jeffries, A. D., Meyer, S. S., Weiss, R., Bachner, F. J., Donnelly, J. P., Lindley, W. T., Mountain, R. W., and Silversmith, D. J. (1984). *Appl. Opt.* **23**, 910.
Ershov, M. (1996). *Appl. Phys. Lett.* **69**, 3480.
Ershov, M. (1998). *Appl. Phys. Lett.* **73**, 3432.
Ershov, M., Hamaguchi, C., and Ryzhii, V. (1996). *Jpn. J. Appl. Phys.* **35**, 1395.
Ershov, M., Liu, H. C., Buchanan, M., Wasilewski, Z. R., and Ryzhii, V. (1997a). *Appl. Phys. Lett.* **70**, 414.
Ershov, M., Liu, H. C., Li, L., Buchanan, M., Wasilewski, Z. R., and Ryzhii, V. (1997b). *Appl. Phys. Lett.* **70**, 1828.
Ershov, M., Ryzhii, V., and Hamaguchi, C. (1995). *Appl. Phys. Lett.* **67**, 3147.
Ershov, M., Satou, S., and Ikebe, Y. (1999). *J. Appl. Phys.* **86**, 6642.
Fathololoumi, S., Dupont, E., Ban, D., Graf, M., Laframboise, S. R., Wasilewski, Z. R., and Liu, H. C. (2010). *IEEE J. Quantum Electron.* **46**, 396.
Ferguson, B., and Zhang, X. C. (2002). *Nat. Mater.* **1**, 26.
Fu, Y., Willander, M., Jiang, J., Li, N., Lu, W., and Liu, H. C. (2003). *J. Appl. Phys.* **93**, 9432.
Fukada, E., and Furukawa, T. (1981). *Ultrasonics* **19**, 31.
Fung, S., Panda, S., and Panda, B. K. (1999). *J. Phys. Condens. Matter* **11**, 1353.
Gornik, E. (1984). *Physica B+C* **127**, 95.
Goss, A. J., Nixon, R. D., Watton, R., and Wreathall, W. M. (1984). *GEC J. Res.* **2**, 198.
Graf, M., Dupont, E., Luo, H., Haffouz, S., Wasilewski, Z. R., SpringThorpe, A. J., Ban, D., and Liu, H. C. (2009). *Infrared Phys. Technol.* **52**, 289.
Graf, M., Scalari, G., Hofstetter, D., Faist, J., Beere, H., Linfield, E., Ritchie, D., and Davies, G. (2004). *Appl. Phys. Lett.* **84**, 475.
Grant, P. D., Laframboise, S. R., Dudek, R., Graf, M., Bezinger, A., and Liu, H. C. (2009). *Electron. Lett.* **45**, 952.
Gunapala, S. D., Bandara, S. V., Liu, J. K., Hill, C. J., Rafol, S. B., Mumolo, J. M., Trinh, J. T., Tidrow, M. Z., and Levan, P. D. (2005). *Proc. SPIE* **5783**, 789.
Gunapala, S. D., Bandara, S. V., Singh, A., Liu, J. K., Rafol, S. B., Luong, E. M., Mumolo, J. M., Tran, N. Q., Ting, D. Z. Y., Vincent, J. D., Shott, C. A., Long, J., and LeVan, P. D. (2000). *IEEE Trans. Electron Devices* **47**, 963.
Gunnarsson, O., and Lundqvist, B. I. (1976). *Phys. Rev. B* **13**, 4274.
Guo, X. G., Tan, Z. Y., Cao, J. C., and Liu, H. C. (2009). *Appl. Phys. Lett.* **94**, 201101.
Haller, E. E. (1994). *Infrared Phys. Technol.* **35**, 127.
Haller, E. E., Hueschen, M. R., and Richards, P. L. (1979). *Appl. Phys. Lett.* **34**, 495.
Heitmann, D., Kotthaus, J. P., and Mohr, E. G. (1982). *Solid State Commun.* **44**, 715.
Helm, M. (2000). The basic physics of intersubband transitions. in: "Intersubband Transition in Quantum Wells: Physics and Device Applications I", edited by Liu, H. C., and Capasso, F., Academic, San Diego, CA.
Hewageegana, P., and Apalkov, V. (2008). *Infrared Phys. Technol.* **51**, 550.
Hosako, I., Sekine, N., Patrashin, M., and Yasuda, H. (2007). *Proc. SPIE* **6772**, 67720R.

Ikonic, Z., Milanovic, V., and Tjapkin, D. (1989). *Appl. Phys. Lett.* **54**, 247.
Jastrow, C., Münter, K., Piesiewicz, R., Kürner, T., Koch, M., and Kleine-Ostmann, T. (2008). *Electron. Lett.* **44**, 213.
Jovanović, V. D., Harrison, P., Ikonić, Z., and Indjin, D. (2004). *J. Appl. Phys.* **96**, 269.
Kane, M. J., Millidge, S., Emeny, M. T., Lee, D., Guy, D. R. P., and Whitehouse, C. R. (1992). in: "Intersubband Transitions in Quantum Wells." edited by Rosencher, E., Vinter, B., and Levine, B. F., (Plenum, New York), pp. 31–42.
Klingshirm, C. F. (1997). "Semiconductor Optics." Springger-Verlag, Berlin.
Kumar, S., Hu, Q., and Reno, J. L. (2009). *Appl. Phys. Lett.* **94**, 131105.
Lake, R., Klimeck, G., Bowen, R. C., and Jovanovic, D. (1997). *J. Appl. Phys.* **81**, 7845.
Lal, R. B., and Batra, A. K. (1993). *Ferroelectrics* **142**, 51.
Levine, B. F. (1993). *J. Appl. Phys.* **74**, R1.
Levine, B. F., Bethea, C. G., Hasnain, G., Shen, V. O., Pelve, E., Abbott, R. R., and Hsieh, S. J. (1990). *Appl. Phys. Lett.* **56**, 851.
Levine, B. F., Choi, K. K., Bethea, C. G., Walker, J., and Malik, R. J. (1987). *Appl. Phys. Lett.* **50**, 1092.
Li, H., Cao, J. C., Han, Y. J., Tan, Z. Y., and Guo, X. G. (2009a). *J. Phys. D Appl. Phys.* **42**, 205102.
Li, H., Cao, J. C., Tan, Z. Y., Han, Y. J., Guo, X. G., Feng, S. L., Luo, H., Laframboise, S. R., and Liu, H. C. (2009b). *J. Phys. D Appl. Phys.* **42**, 025101.
Liu, A. (1994). *Phys. Rev. B* **50**, 8569.
Liu, H. C. (1992). *Appl. Phys. Lett.* **60**, 1507.
Liu, H. C. (1993). *J. Appl. Phys.* **73**, 3062.
Liu, H. C., Buchanan, M., Wasilewski, Z. R., and Chu, H. (1991). *Appl. Phys. Lett.* **58**, 1059.
Liu, H. C., and Capasso, F. (2000). "Intersubband Transitions in Quantum wells: Physics and Device Application I." Academic Press, San Diego.
Liu, H. C., Li, L., Buchanan, M., and Wasilewski, Z. R. (1997). *J. Appl. Phys.* **82**, 889.
Liu, H. C., Luo, H., Song, C. Y., Wasilewski, Z. R., SpringThorpe, A. J., and Cao, J. C. (2007a). *Infrared Phys. Technol.* **50**, 191.
Liu, H. C., Luo, H., Song, C. Y., Wasilewski, Z. R., Thorpe, A. J. S., and Cao, J. C. (2007b). *Infrared Phys. Technol.* **50**, 191.
Liu, H. C., Luo, H., Song, C. Y., Wasilewski, Z. R., Thorpe, A. J. S., and Cao, J. C. (2008). *IEEE J. Sel. Top. Quantum Electron.* **14**, 374.
Liu, H. C., Song, C. Y., SpringThorpe, A. J., and Cao, J. C. (2004). *Appl. Phys. Lett.* **84**, 4068.
Liu, H. C., Song, C. Y., Wasilewski, Z. R., SpringThorpe, A. J., Cao, J. C., Dharma-wardana, C., Aers, G. C., Lockwood, D. J., and Gupta, J. A. (2003). *Phys. Rev. Lett.* **90**, 077402.
Luo, H., Laframboise, S. R., Wasilewski, Z. R., Aers, G. C., Liu, H. C., and Cao, J. C. (2007). *Appl. Phys. Lett.* **90**, 041112.
Luo, H., Liu, H. C., Song, C. Y., and Wasilewski, Z. R. (2005). *Appl. Phys. Lett.* **86**, 231103.
Luo, H., Liu, H. C., Song, C. Y., Wasilewski, Z. R., and SpringThorpe, A. J. (2006). *Proc. SPIE* **6386**, 638611.
Patrashin, M., and Hosako, I. (2008). *Opt. Lett.* **33**, 168.
Patrashin, M., Hosako, I., and Merken, P. (2006). *Proc. SPIE* **6038**, 60380H.
Perera, A. G. U. (2006). *Opto-electron. Rev.* **14**, 103.
Perera, A. G. U., Shen, W. Z., Liu, H. C., Buchanan, M., and Schaff, W. J. (2000). *Mat. Sci. Eng. B-SOLID* **74**, 56.
Petrov, A., and Shik, A. (1998). *J. Appl. Phys.* **83**, 3203.
Richards, P. L. (1994). *J. Appl. Phys.* **76**, 1.
Ryzhii, M., and Ryzhii, V. (1998). *Appl. Phys. Lett.* **72**, 842.
Ryzhii, M., Ryzhii, V., and Willander, M. (1998). *J. Appl. Phys.* **84**, 3403.

Ryzhii, V. (1997). *J. Appl. Phys.* **81**, 6442.
Scalari, G., Walther, C., Fischer, M., Terazzi, R., Beere, H., Ritchie, D., and Faist, J. (2009). *Laser & Photon. Rev.* **3**, 45.
Schneider, H., Fleissner, J., Rehm, R., Walther, M., Pletschen, W., Koidl, P., Weimann, G., Ziegler, J., Breiter, R., and Cabanski, W. A. (2003). *Proc. SPIE* **4820**, 297.
Schneider, H., Koidl, P., Schönbein, C., Ehret, S., Larkins, E. C., and Bihlmann, G. (1996). *Superlattices Microstruct*. **19**, 347.
Schneider, H., and Liu, H. C. (2006). "Quantum well infrared photodetectors: Physics and applications." Springer, Berlin.
Schneider, H., Liu, H. C., Winnerl, S., Song, C. Y., Walther, M., and Helm, M. (2009). *Opt. Express* **17**, 12279.
Schneider, H., Schönbein, C., Walther, M., Schwarz, K., Fleissner, J., and Koidl, P. (1997). *Appl. Phys. Lett.* **71**, 246.
Schönbein, C., Schneider, H., Bihlmann, G., Schwarz, K., and Koidl, P. (1996). *Appl. Phys. Lett.* **68**, 973.
Shen, Y. R. (1984). "The principles of nonlinear optics." John Wiely & Sons, New York.
Spitzer, W. G., and Panish, M. B. (1969). *J. Appl. Phys.* **40**, 4200.
Stillman, G. E., Wolfe, C. M., and Dimmock, J. O. (1970). *J. Phys. Chem. Solids* **31**, 1199.
Tan, Z. Y., and Cao, J. C. (2008). *Physics* **37**, 199.
Tan, Z. Y., Guo, X. G., Cao, J. C., Li, H., and Han, Y. J. (2010). *Acta Phys. Sin.* **59**, 2391.
Tan, Z. Y., Guo, X. G., Cao, J. C., Li, H., Wang, X., Feng, S. L., Wasilewski, Z. R., and Liu, H. C. (2009). *Semicond. Sci. Technol.* **24**, 115014.
Thibaudeau, L., Bois, P., and Duboz, J. Y. (1996). *J. Appl. Phys.* **79**, 446.
Todorov, Y., and Minot, C. (2007). *J. Opt. Soc. Am. A* **24**, 3100.
Tonouchi, M. (2007). *Nat. Photon.* **1**, 97.
West, L. C., and Eglash, S. J. (1985). *Appl. Phys. Lett.* **46**, 1156.
Williams, B. S., Callebaut, H., Kumar, S., Hu, Q., and Reno, J. L. (2003). *Appl. Phys. Lett.* **82**, 1015.
Xiong, F., Guo, X. G., and Cao, J. C. (2008). *Chin. Phys. Lett.* **25**, 1895.
Yang, J., Ruan, S. C., and Zhang, M. (2008). *Chin. Opt. Lett.* **6**, 29.
Yang, Y., Liu, H. C., Shen, W. Z., Li, N., Lu, W., Wasilewski, Z. R., and Buchanan, M. (2009). *IEEE J. Quantum Electron.* **45**, 623.
Załużny, M. (1993). *Phys. Rev. B* **47**, 3995.
Zhang, J., and Potz, W. (1990). *Phys. Rev. B* **42**, 11366.
Zhang, R., Guo, X. G., and Cao, J. C. (2011). *Acta Phys. Sin.* **60**, in press.